3-12-2008

A Comparison of Moiré Interferometry And Digital Image Correlation

Ryan J. Davidson

A COMPARISON OF MOIRÉ INTERFEROMETRY AND DIGITAL IMAGE CORRELATION

THESIS

Ryan J. Davidson, Captain, USAF

AFIT/GAE/ENY/08-M06

DEPARTMENT OF THE AIR FORCE
AIR UNIVERSITY

AIR FORCE INSTITUTE OF TECHNOLOGY

Wright-Patterson Air Force Base, Ohio

The views expressed in this thesis are those of the author and do not reflect the official policy or position of the United States Air Force, Department of Defense, or the U.S. Government.

AFIT/GAE/ENY/08-M06

A COMPARISON OF MOIRÉ INTERFEROMETRY AND DIGITAL IMAGE CORRELATION

THESIS

Presented to the Faculty

Department of Aeronautics and Astronautics

Graduate School of Engineering and Management

Air Force Institute of Technology

Air University

Air Education and Training Command

In Partial Fulfillment of the Requirements for the

Degree of Master of Science in Aeronautical Engineering

Ryan J. Davidson, BS

Captain, USAF

March 2008

AFIT/GAE/ENY/08-M06

A COMPARISON OF MOIRÉ INTERFEROMETRY AND DIGITAL IMAGE CORRELATION

Ryan J. Davidson, BS

Captain, USAF

Approved:

Anthony Palazotto (Chairman) — 12 Mar 08 — Date

Marina Ruggles-Wrenn (Member) — 3/12/08 — Date

Greg Schoeppner (Member) — 12 Mar 08 — Date

Abstract

This research determines the effect of two parameters; subset size and step size, on the accuracy and spatial resolution of digital image correlation. Furthermore, it compares and contrasts digital image correlation and moiré interferometry. Both methods are displacement measurement techniques capable of producing displacement data for every point in a field of view.

Two specimens were tested for this study. The first was an aluminum bar, the second was a graphite/epoxy coupon with a ply structure designed to ensure large inter-laminar strains and strain gradients. Each specimen was tested using both digital image correlation and moiré interferometry

To My Wife and Parents

Acknowledgments

I would like to express my sincere appreciation to my faculty advisor, Dr. Anthony Palazotto. His insight and expertise were instrumental in producing this thesis. I would also like to thank my sponsor, Dr. David Mollenhauer, from the Air Force Research Laboratory for teaching me the intricacies of moiré interferometry and experimental mechanics. His guidance and support were essential to the experimental aspects of this project. Additionally, Jay Anderson and his staff gave me invaluable assistance by providing AFIT's ARAMIS digital image correlation system on a moment's notice when no other cameras were available.

Ryan J. Davidson

Table of Contents

List of Figures

List of Tables

A COMPARISON OF MOIRÉ INTERFEROMETRY
AND DIGITAL IMAGE CORRELATION

I. Introduction

Motivation

Moiré Interferometry, used as a displacement measurement technique is a mature technology. It has been thoroughly studied and documented. Moiré Interferometry is capable of very accurate displacement measurement in translation, rotation and even in deformation. Furthermore, it is capable of giving displacement fields over large areas. However, even though the method is very powerful, it has significant constraints on its use. Moiré interferometry can be used only on flat surfaces or on surfaces with curvature in only one direction. Test specimen preparation is very time intensive. The method is sensitive to even minor flaws in the coatings used. Analysis of results is very tedious and time intensive. Last, the method is so sensitive that the experimental setup must be isolated from the environment.

Digital Image Correlation (DIC) is another full field displacement measurement technique. It is quite new, having first been investigated in the late 1970's. The method can be used to analyze complex geometries, including surfaces with compound curves. Specimen preparation is minimal. DIC software is commercially available and performs much of the analysis of the data, thus DIC is quick and easy. However, the researcher has little insight into the internal processes of the method. Also, the technique is fairly

new, and thus its limitations have not yet been fully explored in the available literature. It is becoming very important to explore the limitations of DIC, as the method is being used more and more in the field of experimental mechanics.

Research Focus

This study had two main objectives. First, an investigation of the effect of two DIC parameters; subset size and step size, on the accuracy and spatial resolution of the method was investigated. These parameters were varied in an attempt to determine the combination that yielded the finest resolution. These results were then compared to results achieved with moiré interferometry. The second objective was to perform a comparison of the strengths and weaknesses of DIC and moiré interferometry. The end result of this comparison should provide guidance to researchers trying to decide which method to use.

Background

The main focus of this study was to present a comparison of DIC and moiré interferometry; thus, a short history of both methods would be beneficial to the understanding of the development, strengths and weaknesses of each method. For moiré interferometry this background will be presented by topic, for DIC the background will be presented in a mostly chronological fashion.

Moiré Interferometry.

The word moiré comes from the French for *watered*, for the shimmer that occurs on the surface of a body of water. Moiré silks display this pattern of shimmering bars created by the superposition of two families of almost parallel lines. In silks, the pattern is made when a piece of the silk; which has a glossy finish but also contains distinct

parallel threads in the weave, is folded upon itself and pressed. The effect of this pressing is to emboss the pattern of the parallel threads of one side into the other. (Oster and Nishijima, 1963) When applied to experimental mechanics through geometrical moiré or moiré interferometry, the moiré effect results in a contour map of equal displacements. This displacement data can be used to determine strains on the surface of a specimen.

The origins on moiré as a measurement technique can be found in the writings of Lord Rayleigh in which he discussed the manufacture of diffraction gratings. While most of the focus of these papers was on the reproduction of gratings, he did note that if two gratings were placed together the gratings would produce a third set of lines, and that these lines could be used to measure the distance between grating lines. (Rayleigh, 1874) This observation was one of the first times that the use of fringe patterns as a measurement technique was suggested. The nearly vertical bars of Figure 1.1 are an example of the effect noted by Rayleigh. These bars are now referred to as moiré fringes.

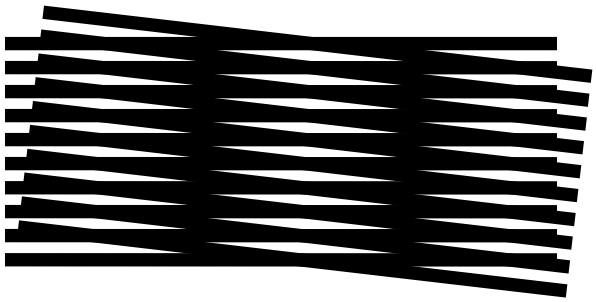

Figure 1.1 Moiré Effect As Discussed by Rayleigh

Some work was done in the early 1900's with the phenomenon that Rayleigh noted, but large scale development of moiré methods did not take place until the 1950's and 1960's. In his review of moiré interferometry Walker noted that Guild's 1954 book *The Interference System of Crossed Diffraction Gratings* is the basis of the modern methods

of moiré interferometry. However, Guild's work was written from the point of view of the mathematician not that of the mechanics experimentalist. It was not until researchers reached the limit of the fineness of physical gratings and hence the spatial resolution of geometrical moiré that Guild's work was further explored. (Walker, 1994)

Typical geometrical moiré experimental setups contained two physical gratings: the specimen grating, which was attached to and deformed with the specimen; and the reference grating, which overlaid the specimen grating but was not attached to the specimen or specimen grating. Fringes were created from the two gratings working in concert to block light transmission through the system. This work was noted for gratings with frequencies on the order of 40 lines per mm; very course by today's standards, and insensitive to small deformations. (Post, 1982)

The advent of the laser enabled a new method of producing the moiré effect. This new method; known as both high-sensitivity moiré and moiré interferometry, produced much finer detail and was capable of resolving much smaller deformations than had previously been shown. Moiré interferometry makes use of one physical grating and one virtual grating. The physical grating is attached to and deforms with the specimen as with geometrical moiré; however, it typically is a reflective film with line densities from 1000 to 4000 lines per mm; 1200 lines per mm is a common density. An example of this type of grating is shown in Figure 1.2. The virtual grating was created through the interaction of two beams of laser light. The two beams of laser light were typically split from one beam using a splitting device. (Post, 1982) Light diffracted from the specimen grating further interacted with the virtual grating, producing the fringe pattern. It should be noted that while moiré interferometry made use of the interference of light to create

fringe patterns, and low-sensitivity moiré used the mechanical interference of the two gratings, the two methods can be described with the same theory, and even the same equations.

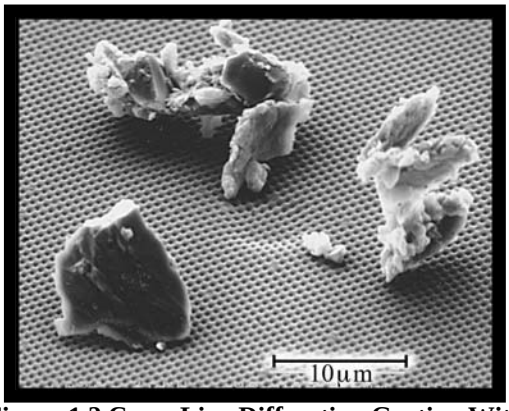

Figure 1.2 Cross Line Diffraction Grating With Dust Particles (Provided by David Mollenhauer and Gary Price)

A two beam interferometer; as described above, would be capable of mapping the deformation in the X direction (U field) or the Y direction (V field), but not both. The deformation field captured would depend on the orientation of the reference and virtual gratings. In a paper published in 1985, Post described a four beam interferometer capable of creating U and V displacement fields in sequential tests. The four beam interferometer is in essence a combination of two, two beam interferometers. The axes of the two interferometers would be the same; however, there would be a 90 degree rotation between the two. The specimen grating used with four beam interferometers would be characterized by furrows in both the X and Y directions. (Post, 1985) Figure 1.2 is an example of a cross line diffraction grating.

The four beam interferometer is a tool well suited to the investigation of strain. While the two beam interferometer is capable of determining normal strain in either the X or Y direction at any point in the field of view, the four beam interferometer can be used to

find strains in both directions. Additionally, the four beam interferometer provides the information to calculate shear strains at any point in the field of view.

While moiré interferometry provides full field data, there is a lower limit to the displacement that it can resolve. However, Weissman and Post demonstrated excellent fringe clarity very near the theoretical limit. Their study showed a sensitivity to displacement of 0.25μm per fringe; 97.6 percent of the theoretical limit of moiré interferometry's sensitivity for the wavelength of light used in the study. (Weissman and Post, 1982) Given the sensitivities possible with moiré interferometry, it should be no surprise that isolation of the interferometer and specimen from all disturbances is crucial. Not only is moiré interferometry capable of registering mechanical disturbances, it is also susceptible to acoustic vibrations, temperature gradients and even air currents. (Han et al., 2001)

One of the major drawbacks of moiré interferometry was the tedious and somewhat subjective nature of analyzing fringes by hand. However, some progress has been made in automating the fringe analysis process. This automation mainly fell into two categories: Fourier transform and stepped phase analysis. Both methods revolve around finding the phase information of the fringe pattern. The Fourier method makes use of a carrier pattern induced into both the null field and the field produced by a load on the specimen. (De Nicola et al., 2000) Lassahn et al. presented two methods for the stepped phase method; the line drawing method, and the beam shuttering method. Both methods require multiple photographs of the fringe pattern for each load case with phase shifts induced between each photograph. The line-drawing method was found to be less sensitive to noise in the raw data, but required more user interaction. (Lassahn et al.,

1994) The line drawing method was used for analysis of moiré data in the present study. The technique will be presented in greater detail in Chapter 2.

Recent research at the United States Air Force Research Laboratory (AFRL) investigated effects of the grating thickness on strains measured with moiré interferometry. It was noted that measured normal transverse strains (ε_{zz}) were greater than that predicted by the AFRL's B-spline Analysis Method (B-SAM). Experimentally measured strains and those determined by B-SAM were much closer when the B-SAM models were modified to include the thickness and stiffness of the grating as shown in Figure 1.3. Variations of out of plane displacements due to the grating were the proposed mechanism for this amplification. (Mollenhauer et al., in press)

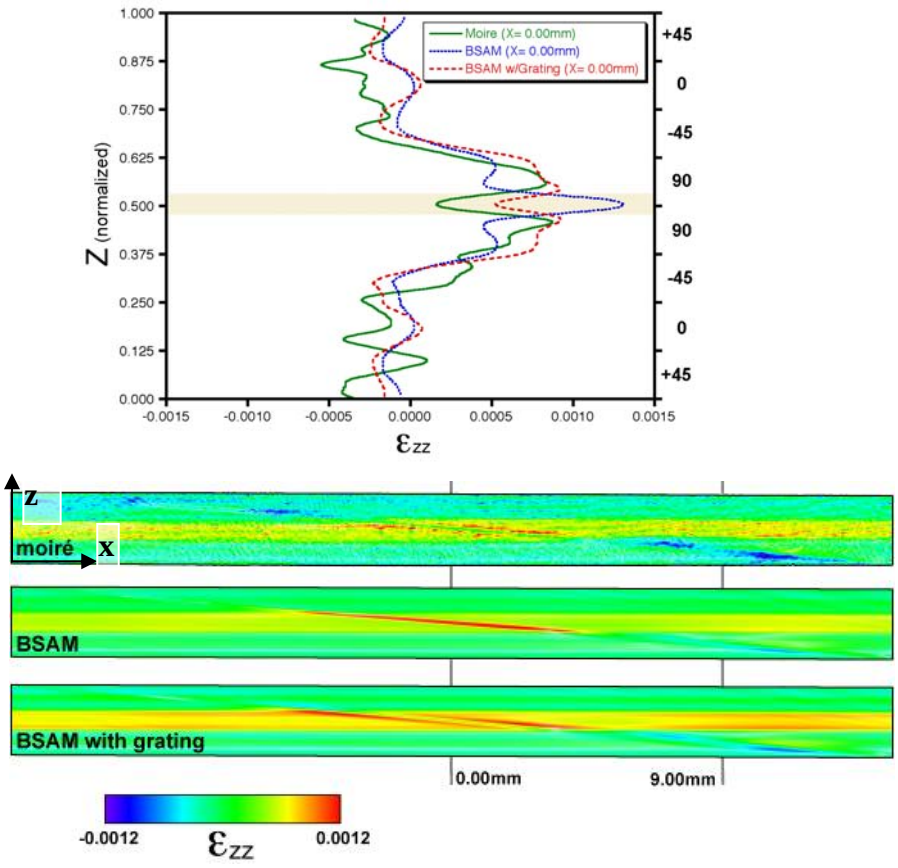

Figure 1.3 Specimen Grating Thickness Effects on Transverse Strain (Mollenhauer et al., in press)

Digital Image Correlation.

Digital image correlation is a method of determining displacement fields by tracking the movement of points on the surface of a specimen during loading. The surface is first broken down into many overlapping areas. These overlapping areas are called subsets. The subset is typically square, and the size of the subset is defined by the user. The DIC program used for the research presented in this thesis (Correlated Solutions' Vic-3D 2006) allowed the user to set the size of the subset between 10 and 100 pixels. The points that are tracked are the centers of the subsets. The side of each subset is separated from the corresponding side of the previous subset by a distance called the step size. Vic-3D 2006 allowed step sizes to be user defined between 1 and 50 pixels. High resolution digital cameras are used to capture photographs of the specimen before and during (or after) loading. The center of the subsets are tracked instead of random points because the pattern in the subset will be statically unique, as opposed to individual points that appear very similar to one another. If the position of many subsets centers can be tracked from the photograph of an unloaded specimen to the photograph of the loaded specimen a deformation field can be generated.

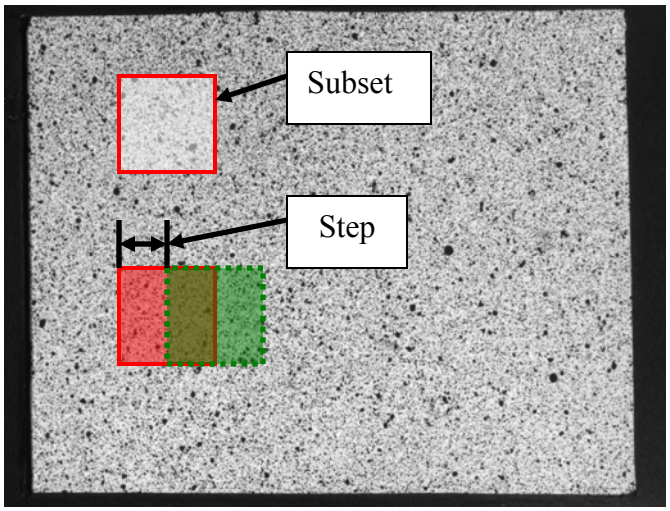

Figure 1.4 Subset Size and Step Size

Investigation of digital image correlation began in the early 1980's. In 1983 Sutton et al., presented a review of the theory of DIC, and introduced an improved numerical method for determining an object's deformation. This paper noted that intensity data on a sub-pixel scale would be required to accurately determine deformations and that an interpolation of the recorded intensity field would render data between integer pixel locations. A bi-liner interpolation scheme was used to interpolate the intensity values. After obtaining the sub-pixel data, displacement of points on the surface could be determined. A correlation coefficient was used to compare a particular subset of the undeformed data set and a candidate subset of the deformed data set. The candidate subset of the deformed data that minimized the correlation coefficient was assumed to represent the same area on the surface of the deformed object as that of the subset from the undeformed data set. (Sutton et al., 1983)

One of the major limitations of DIC was the excessive processing time required to converge on a solution using the then standard search method: course-fine search. The course-fine search was an iterative numerical method that initially used large step sizes to find an area where a solution could exist, then used smaller step sizes to find the solution. (Chu et al., 1985, 237-238) Bruck, et al., presented a method to reduce this processing time. Like Sutton, Bruck used an interpolation scheme to obtain sub-pixel intensity resolutions. However, instead of using the course-fine approach of Sutton, Bruck used a process based on the Newton-Raphson method of partial differential corrections. The Newton-Raphson method calculated corrections to an initial estimate of the solution. The method was iterative, so new corrections were made until the estimate converged to a solution. Bruck proved the Newton-Raphson method provided accurate results for the

displacements and displacement gradients with less computational time required. However, it was subject to many of the same limitations of other iterative numerical methods. (Bruck et al., 1989)

The late 1980's and early 1990's saw the extension of DIC from a two dimensional in-plane method to a three dimensional method which was capable of determining out of plane deformations. Kahn-Jetter and Chu theorized that photographs taken from two perspectives coupled with photogrammetric principles could be used to add a depth measurement to DIC. To achieve out of plane capability, the point of interest must be present in both photographs and additionally it must also be in focus in both photographs. Kahn-Jetter and Chu found that the use of stereoscopic machine vision with DIC provided very accurate and reliable results for displacement measurement in three dimensions. (Kahn-Jetter and Chu, 1990)

Kahn-Jetter and Chu's experimental set-up was such that they used one camera that was moved to give the perspective needed for depth sensing. The camera was placed such that the axis of the camera was parallel in both positions. Luo et al., tested an experimental set-up which used two cameras with an angle between the axes of the cameras. Additionally, Luo et al. transformed the coordinates of a point on the object of interest in global coordinates to a location of the image plane of two cameras. This transformation was a function of twelve parameters associated with the cameras and their orientation. These twelve parameters were determined through a calibration technique. The calibrated system was then able to relate the position of a point in the two sensor planes of the camera to the three dimensional global coordinate system. Luo et al.

determined that the accuracy and standard deviation of this system was approximately 0.08 pixel and 0.06 pixel respectively. (Luo et al., 1993)

In two articles Helm, Sutton and McNeill presented a new method of calibration of the twin camera three dimensional DIC setup. While their camera model paralleled that of Luo et al. the model of Helm et al. was composed of eleven parameters as opposed to twelve. The determination of these eleven parameters would calibrate the system. Helm further realized that one of the parameters; the sensor plane aspect ratio, was hard wired into the camera. If the camera's computer and digitizing board were unchanged, the aspect ratio would remain unchanged irrespective of the rest of the experimental setup. The aspect ratio could be determined independently from the other ten parameters. The camera model and calibration method of Helm was found to be superior to that of Lou because it contained a correction for perspective, thus allowing more flexibility in camera placement. Just as importantly, Helm's method was much faster and simpler to perform. (Helm et al., 1994; Helm et al., 1996) Helm's work will be presented in detail in Chapter 2.

Comparison of Digital Image Correlation and Moiré Interferometry.

To date, little has been published on direct comparisons between DIC and moiré interferometry. However, David Mollenhauer of the AFRL and John Tyson of Trillion Quality Systems conducted just such a comparison in 2004. They performed the comparison on a very architecturally complex preformed-pi composite T-joint as depicted in Figure 1.5. They first conducted moiré tests, then applied a speckle pattern over the diffraction grating and performed digital image correlation tests. Mollenhauer and Tyson concluded that the spatial resolution of the moiré interferometry technique was much

higher than that of digital image correlation with the subset size and step used. The resolution of digital image correlation was highly dependent on the subset size and step. They then re-sampled the moiré data to match the resolutions of the two methods and analyzed the data again. Trends in strain were noted to be similar, but digital image correlation showed some strains that were not present in either the full or reduced resolution moiré data. (Mollenhauer and Tyson, 2004)

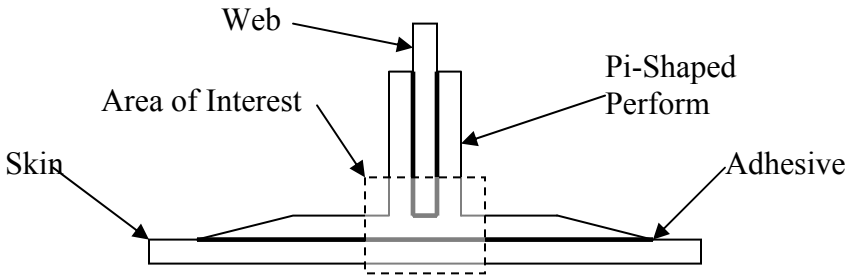

Figure 1.5 Preformed-Pi Composite T Joint

Thesis Overview

The objectives of this study were to determine how subset size and step size influence the spatial resolution of DIC and to compare the strengths and weaknesses of each method. Chapter Two presents the theory germane to the discussion of both moiré interferometry and digital image correlation.

Chapter Three details the manufacture of the two specimens used in the experimental comparison of moiré and digital image correlation. The first specimen was an aluminum bar. This specimen was used to show the accuracy of DIC when applied to a simple displacement field and to highlight the differences in resources required by DIC and moiré interferometry. The second specimen was a graphite/epoxy composite coupon with a $[-45_2/0_2/45_2/90_2]_S$ unidirectional fiber orientation lay up. This particular layup was used to ensure a very complex strain field. A third specimen had been planned which

would have provided an intermediate level of complexity in the strain field. This third specimen was not tested due to time constraints imposed by equipment failure. The chapter goes on to discuss the experimental method used to gather data, and the techniques used to analyze the gathered data.

Chapter Four presents the results of experimentation. Comparisons of data gathered using moiré interferometry and digital image correlation are presented. Additionally, a numerical model was incorporated in order to provide additional insight into the strain field of the composite specimen. A discussion is carried out of the strengths and weaknesses of each method, and also how these strengths and weaknesses affect the use of the particular technique.

Conclusions based on the experimental data and recommendations for further research in this area are presented in Chapter Five.

II. Theory

Moiré Interferometry

Moiré interferometry was developed in order to determine the axial, transverse and shear strains on the surface of a specimen. The product of the interferometer is not a strain field however. The interferometer produces a field of fringes that indicate locations with equal displacement that can then be used to find the strains. Equations to calculate strains are presented later in this chapter along with the basic theory behind moiré interferometry, the theoretical limits of moiré, and the stepped phase method of fringe analysis.

Basic Theory.

The action of moiré interferometry can be thought of as similar to geometric moiré. In geometric moiré, two gratings are superimposed on one another with only one of the gratings attached to the specimen. The gratings typically have either equal spacing between lines, or one grating will have some fraction of the spacing of the other. The case of equal spacing will produce no fringes when the two gratings are aligned. The case of unequal spacing will produce a fringe pattern when the gratings are aligned, even when no load has been placed on the specimen. When the specimen is loaded and undergoes a strain, the grating attached to the specimen will strain with the specimen. In either case new fringes will be created where the lines from the two gratings nearly overlap. The displacement field can then be found through the spacing of the fringes and use of simple geometry.

The similarity between geometric moiré and moiré interferometry allows for an intuitive understanding of moiré interferometry. However, a more rigorous explanation

can be made as discussed in Post, et al. 1994. The diffraction grating attached to the surface of the specimen is illuminated with two laser beams. As shown in Figure 2.1, the two beams impinge on the grating at angles α and -α. The diffraction grating scatters the two beams in many smaller beams traveling at angles β_m to the normal of the grating where the angle of departure of each diffraction order is given by

$$\sin \beta_m = \sin \alpha + m\lambda f_s \tag{1}$$

where:

β_m = Angle of departure of the diffraction order

α = Angle of arrival of the original laser beam

m = The diffraction order

λ = Laser wavelength

f_s = Frequency of the specimen grating

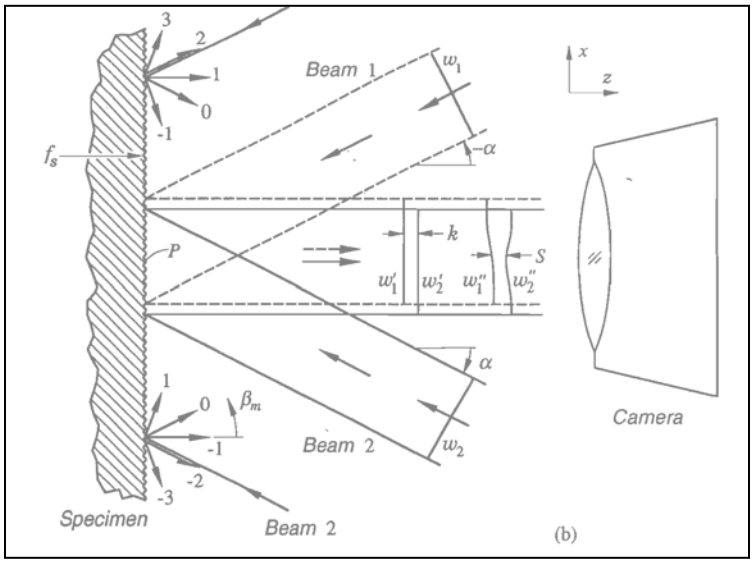

Figure 2.1 Diffraction Orders and Wave Front Interference (Post et al., 1994)

α and -α can be set such that diffraction order 1 of beam one and diffraction order -1 of beam two will reflect perpendicularly from the grating on the surface of the specimen.

When α and - α are set as such, the interaction of the two laser beams in the volume where they cross will produce a virtual grating of frequency f as shown in equation 2.

$$f = \frac{2}{\lambda}\sin\alpha \tag{2}$$

If the specimen grating was replicated perfectly, and there is no load on the specimen the two diffraction orders will have flat wave fronts. Since the reflected beams travel parallel to each other and are flat, the two reflected wave fronts do not interact with each other and no fringe pattern is produced. If the specimen is subjected to a uniform strain; ε, then the specimen grating will strain as well, causing the frequency of the grating to become

$$f_s = \frac{f/2}{1+\varepsilon} \tag{3}$$

From equations 1 and 3, the angles of departure of diffraction order 1 of beam one and diffraction order -1 of beam two become:

$$\beta_1 = -\frac{\lambda f \varepsilon}{2} \qquad\qquad \beta_{-1} = \frac{\lambda f \varepsilon}{2} \tag{4}$$

Since the two wave fronts emerge from the specimen grating at angles to each other they will interact with each other to produce a field of uniformly spaced fringes. If however, the specimen undergoes a non-uniform strain, then the non-uniform deformation of the specimen grating will cause the reflected wave fronts to be warped. These warped wave fronts will interact with each other causing a non-uniformly spaced fringe pattern. The fringe index, or fringe order, N, is dependent on the separation and the wavelength of light used.

Figure 2.2 shows the moiré interferometry experimental setup used for the research presented in this thesis. It should be noted that only one laser is used to generate the four

beams used. The single laser is split into four parts by a beam splitter internal to the interferometer. Two of the four laser beams that illuminate the specimen are blocked for determination of the U displacement field, and the other two are blocked during testing for the V field.

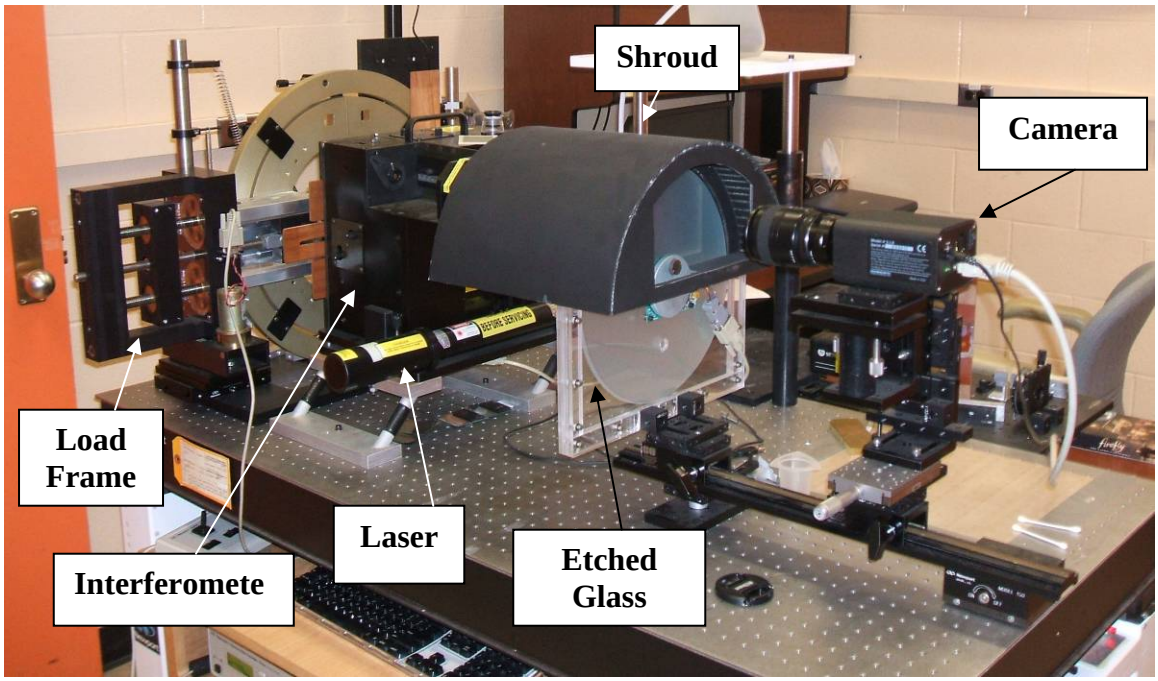

Figure 2.2 Moiré Interferometry Experimental Setup

If the fringe order is known, then it is a simple matter to determine displacement fields:

$$U(x,y) = \frac{1}{f} N_x(x,y) \qquad V(x,y) = \frac{1}{f} N_y(x,y) \qquad (5)$$

where U and V are the displacement fields in the X and Y direction respectively and the subscript on N denotes the moiré field under investigation. It should be noted that N_x and N_y are directly measurable from photographs of the U and V moiré fields. Strains are likewise easy to determine with knowledge of the fringe patterns and the virtual grating frequency:

$$\varepsilon_x(x,y) = \frac{\partial U}{\partial x} = \frac{1}{f}\left(\frac{\partial N_x}{\partial x}\right)$$

$$\varepsilon_y(x,y) = \frac{\partial V}{\partial y} = \frac{1}{f}\left(\frac{\partial N_y}{\partial y}\right) \tag{6}$$

$$\gamma_{xy}(x,y) = \frac{\partial U}{\partial y} + \frac{\partial V}{\partial x} = \frac{1}{f}\left(\frac{\partial N_x}{\partial y} + \frac{\partial N_y}{\partial x}\right)$$

It is often acceptable to substitute $\frac{\Delta N_x}{\Delta x}$ for $\frac{\partial N_x}{\partial x}$, $\frac{\Delta N_y}{\Delta y}$ for $\frac{\partial N_y}{\partial y}$, $\frac{\Delta N_x}{\Delta y}$ for $\frac{\partial N_x}{\partial y}$ and $\frac{\Delta N_y}{\Delta x}$ for $\frac{\partial N_y}{\partial x}$. (Post et al., 1994)

Theoretical Limit.

While moiré interferometry has the capability to resolve exceedingly small displacements it is constrained by the maximum virtual grating frequency attainable. Equation 2 sets the frequency of the virtual grating, and shows that the maximum frequency of the virtual grating for a given wavelength will be achieved when α is set to 90 degrees. Weissman and Post demonstrated excellent fringe patterns could be achieved with a 488 nm laser illuminating the specimen grating at an angle of 77.4 degrees. This equates to a virtual grating of 4000 lines per mm, 97.6 percent of the theoretical maximum for this wavelength.

Stepped Phase Fringe Analysis.

Automation of fringe analysis to determine N_x and N_y can be performed if information about the phase of the fringe pattern intensity is known. The method of undetermined phase shifts presented by Lassahn et al. required k photographs of the fringe pattern be taken, where k is at least three. The phase of one of the two lasers

illuminating the specimen grating is shifted between each photograph. This phase shift gives an intensity pattern described by equation 7.

$$I(x,y) = A(x,y) + B(x,y)\cos(\Phi(x,y) + \Delta_k) \tag{7}$$

where

I(x,y) = intensity at any point in the field of view

A(x,y) = intensity of the two beams

B(x,y) = fringe contrast

Φ(x,y) = phase difference between the two beams

Δ_k = phase shift induced into one beam

To find the phase at any point in the field of view, one must first determine Δ_k, the shift in phase between each photograph. Once Δ_k is known, the folded phase can be found. The folded phase is simply the phase expressed periodically between 0 and 2π. The phase can be unfolded by adding $2\pi L$ to each period.

Using Lassahn's method, one must first find Δ_k. Lassahn presented a complex method for finding the phase shift. The method used in this research to find the phase shift is much simpler than that proposed by Lassahn, although it still requires the researcher to specify a line that crosses one full fringe. The fringe that the line crosses should have as little noise as possible and the phase should vary linearly along the line. The intensity values along the line are extracted from the photographs of the fringe pattern and put into an array. A search routine is run to find the local maxima and minima of the intensity values along the line for each photograph. The spacing between maxima of each photograph is assumed to be the phase shift. Figure 2.3 depicts the phase shift solution for a single phase shift.

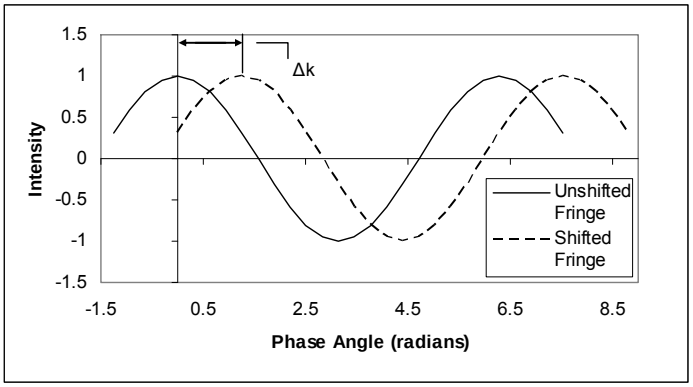

Figure 2.3 Phase Shift Solution

Once Δ_k has been determined, the folded phase Ψ can be found. Returning to the intensity equation; equation 7, substitute $\Phi = \Psi + 2\pi L$. For now neglect the $2\pi L$ term as it will be accounted for later by unfolding the phase. The intensity equation becomes:

$$I_k = A + B\cos(\Psi + \Delta_k) \tag{8}$$

Using the trigonometric identity cos(a + b) = cos(a)cos(b) – sin(a)sin(b), equation 8 becomes

$$I_k = A + B\cos(\Psi)\cos(\Delta_k) - B\sin(\Psi)\sin(\Delta_k) \tag{9}$$

To simplify equation 9, replace A, Bcos(Ψ) and -Bsin(Ψ) with P1, P2 and P3 respectively. I_k becomes

$$I_k = P1 + P2\cos(\Delta_k) + P3\sin(\Delta_k) \tag{10}$$

Since the intensity, I is known for each pixel of the k photographs P1, P2 and P3 can be found if $k = 3$ through solving the system of three equations. However, it is advisable to use more than three photographs. If $k > 3$, then the system will be over determined and can be solved using a linear least squares scheme as follows. First, place the system of equations in matrix equation format:

$$\begin{Bmatrix} I_1 \\ \vdots \\ I_k \end{Bmatrix} = \begin{bmatrix} 1 & \cos\Delta_1 & \sin\Delta_1 \\ \vdots & \vdots & \vdots \\ 1 & \cos\Delta_k & \sin\Delta_k \end{bmatrix} \begin{Bmatrix} P_1 \\ P_2 \\ P_3 \end{Bmatrix} \tag{11}$$

The linear least squares solution of this system of equations is

$$\begin{Bmatrix} P_1 \\ P_2 \\ P_3 \end{Bmatrix} = \left[D^T D\right]^{-1}\left[D^T\right]\{I\} \tag{12}$$

where term D is the coefficient matrix from equation 11. The folded phase is easily found using the expressions defining P_2 and P_3:

$$\tan\Psi = \frac{-B\sin\Psi}{B\cos\Psi} = \frac{P3}{P2} \tag{13}$$

thus:

$$\Psi = \tan^{-1}\left(\frac{P_3}{P_2}\right) \tag{14}$$

Unfolding the phase establishes the link between the stepped phase method and the fringe order discussed earlier. To unfold the phase and find Φ, multiples of 2π are added to the folded phase at each location where the phase goes from 2π to 0. The addition of the 2π term removes the discontinuities in the phase data as shown in Figure 2.4.

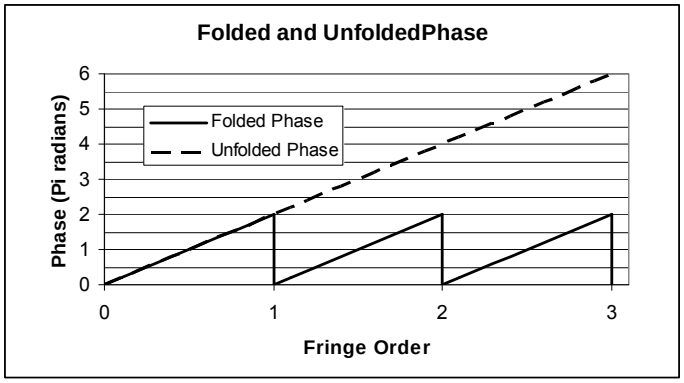

Figure 2.4 Folded and Unfolded Phase

If the intensity peaks at the 0-2π phase discontinuity, then the fringe order will increment at the 0-2π discontinuity. Thus, the multiple, L of the 2π added to the folded phase to unfold it will locate the integer fringe orders. However, if a continuous displacement field is desired, then equation 5 requires the knowledge of not only the integer fringe orders, but knowledge of the non integer fringe orders as well. The unfolded phase contains this information. In fact, the ratio of the unfolded phase to 2π gives the value of the fringe order, integer or non integer.

$$N_x(x,y) = \frac{\Phi_x(x,y)}{2\pi} \qquad N_y(x,y) = \frac{\Phi_y(x,y)}{2\pi} \tag{15}$$

where

$N_x(x,y)$ = The fringe order of the U field

$N_y(x,y)$ = The fringe order of the U field

$\Phi_x(x,y)$ = The unfolded phase of the U field

$\Phi_y(x,y)$ = The unfolded phase of the V field

A program called Superfringe was written by Dr. David Mollenhauer to accept the input of photographs of the U and V interferograms. The program then calculated the unfolded phase. Last, the program output the U and V displacement fields. This program was used in the research described in this thesis.

Digital Image Correlation

Like moiré interferometry, DIC is at its core a displacement measurement technique. Both methods make use of equations 6 to determine strains from the U and V displacement fields. DIC however, uses a vastly different method of determining the displacement fields than moiré interferometry uses. Instead of mapping locations with equal displacement, DIC produces a displacement field by tracking the movement of each

point on the surface of an object while that object is loaded. For a surface with no texture or a uniform texture, each location is indistinguishable from any other point. A speckle pattern can be applied to the surface to provide a means of uniquely identifying every point. A small area is defined around each point on the surface. These areas are known as subsets. For a properly applied speckle pattern each subset will have an arrangement of speckles which is unique from any other subset. If the locations of enough subsets can be found in pictures taken before and after the application of a load, then the displacement field can be determined. An optimization is used to locate each subset in the two photographs.

Figure 2.5 depicts one of the two DIC experimental setups used for the research conducted for this thesis. The item labeled light source was an incandescent light bulb with a housing and two fiber-optic extensions that were used to direct the light onto the specimen. No laser is used with DIC.

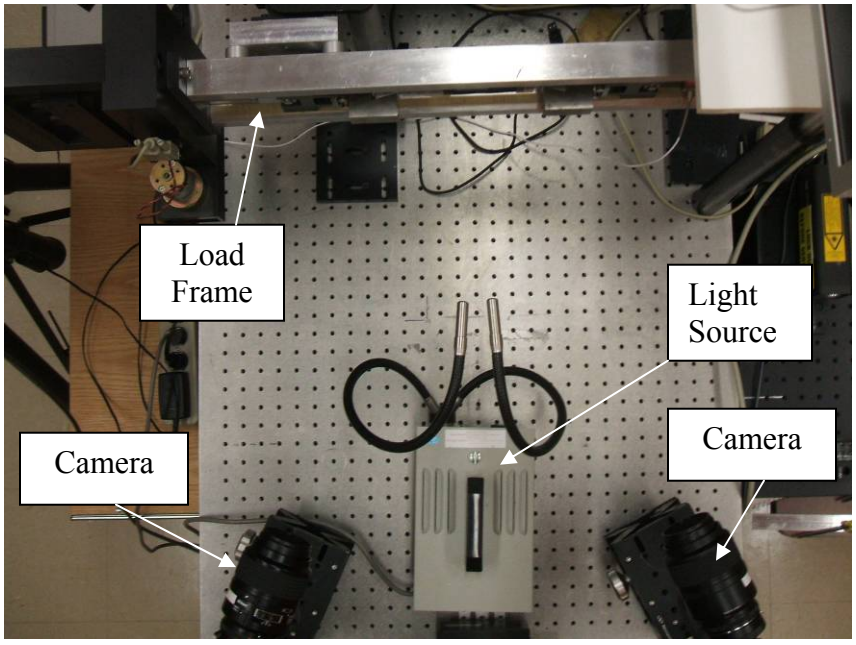

Figure 2.5 DIC Experimental Setup at AFRL

The theory behind DIC is presented below. First, the need for and execution of interpolation to find sub pixel data, then the correlation coefficient and last, the extension of the method to three dimensions are discussed. An attempt has been made to discuss the same methods used in Vic-3D 2006. However as this is a commercial software package, the equations used by the software are proprietary data and may not be the same as those presented below.

Sub Pixel Data.

The modern digital camera's sensor plane is broken into a grid of pixels. Each pixel records the intensity of the light striking the area of the sensor plane covered by that pixel. Because the pixel covers a discrete area, the intensity that is recorded is the average of the intensity across the area of the pixel. This averaging of intensities is shown in Figures 2.6 and 2.7. Figure 2.6 shows the intensity values for a speckle pattern with a 10 by 10 pixel area highlighted. Figure 2.7 shows how the intensity data of the highlighted area are recorded by a digital camera. Note the flattened peaks of the recorded intensity data, versus the jagged peaks of the actual intensity.

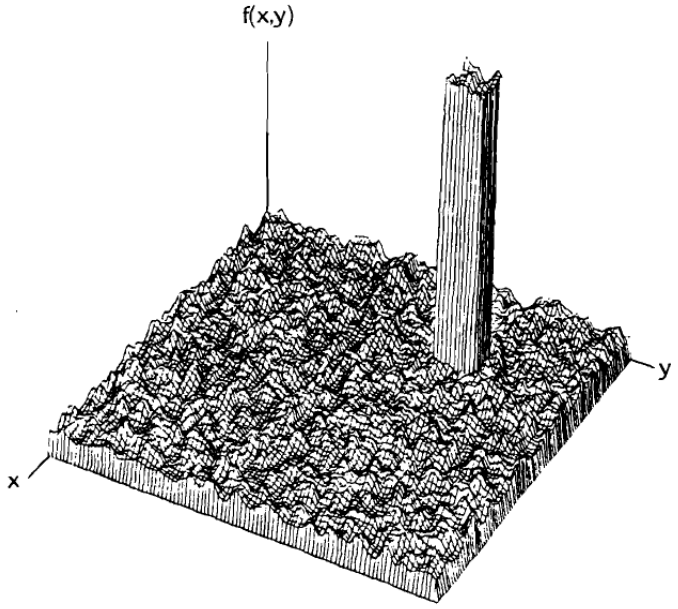

Figure 2.6 Intensity Data With a 10 by 10 Subset Highlighted (Chu et al. , 1985)

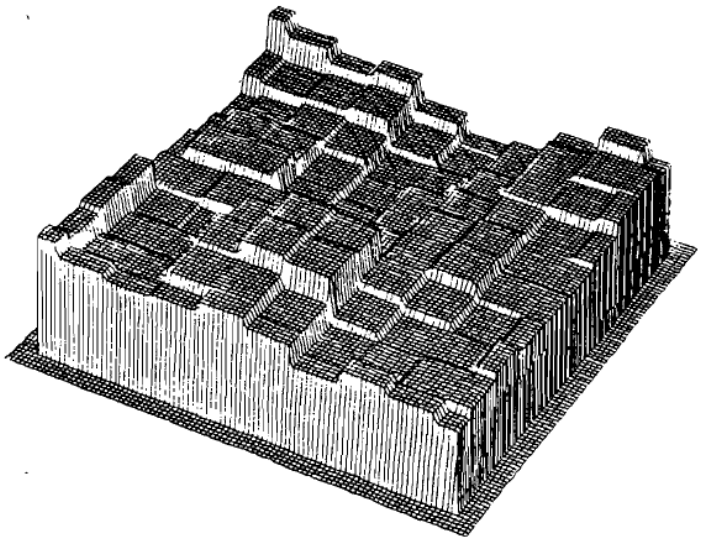

Figure 2.7 Intensity Recorded by a Digital Camera for 10 by10 pixel Subset From Figure 2.4 (Chu et al. , 1985)

If no scheme is used to generate intensity data between pixel centers then the correlation will only be able to provide displacement values at integer pixel locations. (Bing and others, 2006) Furthermore, Bruck et al. found that if only pixel center locations were used, then displacements and displacement gradients would be coupled; a limitation not acceptable for many mechanics problems. (Bruck and others, 1989) Numerous interpolation schemes have been proposed, however, the cubic B-Spline method was used byVic-3D 2006 in the experiments described in Chapter 3. B-Spline interpolation is based on fitting a function through known data points. The value of the function C at the point of interest is the interpolated value. The function is a sum of basis functions; $b_{i,p}$, multiplied by control points P_i.

$$C = \sum P_i b_{i,p} \tag{16}$$

Each basis function will span four intervals, and is a piecewise defined function comprised of four cubic polynomials. The polynomials that make up the basis function must have equal values where they intersect, and the first and second derivatives must also be equal at intersection points. The polynomials used to define the basis functions are as follows:

$$b_{i,0} = \begin{cases} 1 \quad if \quad t_i \le t < t_{i+1} \quad and \quad t_i < t_{i+1} \\ 0 \quad Otherwise \end{cases}$$

$$b_{i,p} = \frac{t - t_i}{t_{i+p} - t_i} b_{i,p-1} + \frac{t_{i+p+1} - t}{t_{i+p+1} - t_{i+1}} b_{i+1,p-1} \tag{17}$$

In equation 17, t is the knot value. The control points act as a weighting factor and shift the particular basis function up or down. Unlike the polynomials that make up the basis functions, the values of the control points must be determined. The control points can be

found using the fact that the function produced by the b-spline must go through the known data points. This condition sets up a system of equations that can be solved to determine the control points. (Iarve, 2008; Weisstein, 2008)

Correlation Coefficient.

The heart of any image correlation method is the correlation scheme. The correlation coefficient compares a reference photograph to another photograph. Often the second photograph will show the object in the reference photograph after a load has been applied to the object. Many such schemes have been presented in the literature, but the technique used by Correlated Solutions in Vic-3D 2006 was a Normalized Sum of Squared Differences (NSSD). A sum of squared differences technique compares the intensity values between the two photographs. A subset from the reference image is used as the benchmark data to which candidate subsets from the deformed image are compared. The candidate subset with the minimum correlation coefficient is assumed to represent the same location on the deformed surface as the reference subset on the undeformed surface. The NSSD method is very similar, except that the intensity values are normalized by the average intensity value for the image. Equation 18 is an expression expected to be similar to that used by Vic-3D 2006.

$$c(x,y,u,v)=\sum_{i,j=-n/2}^{n/2}\left(\frac{I(x+i,y+j)}{I_{AVE}}-\frac{I^{*}(x++u+i,y+u+j)}{I_{AVE}}\right)^{2} \tag{18}$$

where

c = correlation coefficient

x = reference image pixel abscissa location

y = reference image pixel ordinate location

n = subset size

I = reference image pixel intensity

I^* = after deformation image pixel intensity

I_{AVE} = average intensity value

Three Dimensional DIC System.

The application of DIC to determine displacements in three dimensions requires a method of depth measurement. Photogrammic principles give this capability. In short, these principles determine depth by comparing the location of a feature visible in two photographs taken from different perspectives. The camera model and the geometry of the two cameras with respect to each other are the keys to this method. Five internal parameters: the pin hole distance (phd), location of image center (C_x, and C_y), lens distortion factor κ, and aspect ratio (AR) and six external parameters: ζ, η, ξ, X_0, Y_0, Z_0; (which describe the location and orientation of the cameras) define the camera model. (Helm, et al., 1994) The determination of these eleven parameters is known as the calibration of the system.

As presented by Helm et al., the seven coordinate systems shown in Figure 2.8 are used to relate the location of a point in space to locations in the two images captured with the camera sensors. The SYS coordinate system is attached to the object of interest. The pin holes of cameras one and two are located at the origin of systems CAM_1 and CAM_2 respectively. The axis of each camera is aligned with the Z axis of its respective coordinate system. Each camera sensor has a coordinate system associated with it, SEN_1 and SEN_2 as does each image produced by the cameras: IMG_1 and IMG_2. The origins of the SEN and IMG systems are located in the same plane, but are not co-located.

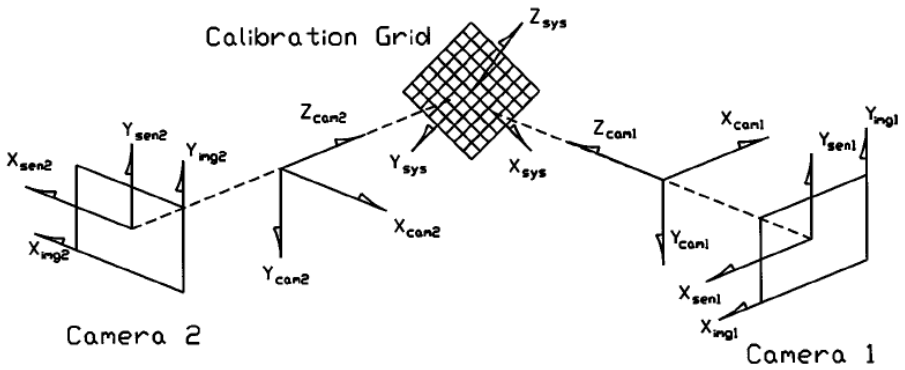

Figure 2.8 Coordinate Systems Used to Relate Locations in Space to Locations in DIC Images (Helm et al., 1996)

If the camera coordinate systems are initially aligned with the SYS coordinate system, locations in the SYS coordinate system can be transformed into each camera coordinate system by a series of three rotations of the respective camera coordinate system and one translation of the SYS system. The first rotation; ζ, occurs about the Z_{SYS} axis. The second rotation; η, occurs about the Y_{SYS} axis. The third rotation; ξ, occurs about the X_{SYS} axis. Rotations must occur in this order. These rotations can be depicted as a rotation matrix R as follows:

$$[R] = \begin{bmatrix} \cos\zeta\cos\eta & -\sin\zeta\cos\eta & \sin\eta \\ \sin\zeta\cos\xi + \cos\zeta\sin\eta\cos\xi & \cos\zeta\cos\xi - \sin\zeta\sin\eta\sin\xi & -\cos\eta\sin\xi \\ \sin\zeta\sin\xi - \cos\zeta\sin\eta\cos\xi & \cos\zeta\sin\xi + \sin\zeta\sin\eta\cos\xi & \cos\eta\cos\xi \end{bmatrix} \quad (19)$$

where

R = Rotation Matrix

ζ = the rotation about the Z_{SYS} axis

η = the rotation about the Y_{SYS} axis

ξ= the rotation about the X_{SYS} axis

The translation of the SYS coordinate system of distances X_0, Y_0 and Z_0 are shown in vector form:

$$[T] = \begin{bmatrix} X_0 \\ Y_0 \\ Z_0 \end{bmatrix} \tag{20}$$

where

T = translation vector

X_0 = translation in SYS_X direction

Y_0 = translation in SYS_Y direction

Z_0 = translation in SYS_Z direction

Thus, the transformation to camera coordinates from the system coordinates is as follows:

$$\begin{bmatrix} X_{CAM} \\ Y_{CAM} \\ Z_{CAM} \end{bmatrix} = [R] \begin{bmatrix} X_{SYS} \\ Y_{SYS} \\ Z_{SYS} \end{bmatrix} + [T] \tag{21}$$

The next step is to convert the camera coordinate system into the sensor system. This is a simple transformation which makes use of two sets of similar triangles, one for the horizontal coordinates and one for vertical coordinates. Figures 2.9a and 2.9b depict this geometric relationship.

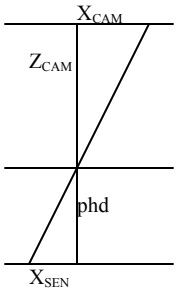

Figure 2.9a Horizontal Geometrical Relation Between CAM and SEN Coordinate Systems

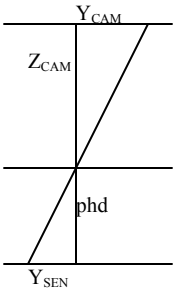

Figure 2.9b Vertical Geometrical Relation Between CAM and SEN Coordinate Systems

Equations 22 are the implementation of this transform.

$$X_{SEN} = \frac{(phd)X_{CAM}}{Z_{CAM}} \qquad Y_{SEN} = \frac{(phd)Y_{CAM}}{Z_{CAM}} \tag{22}$$

The lens system will cause some amount of distortion of the image. However, if the distortion factor κ is known; or in this case can be found, the distortions can be removed from the system via equations 23. The bars over X_{SEN} and Y_{SEN} denote correction of the distortions.

$$\overline{X}_{SEN} = \frac{X_{SEN}}{1 + \kappa\sqrt{X_{SEN}^2} + Y_{SEN}^2} \qquad \overline{Y}_{SEN} = \frac{Y_{SEN}}{1 + \kappa\sqrt{X_{SEN}^2} + Y_{SEN}^2} \tag{23}$$

Finally, the sensor coordinate system; SEN, is transformed to the image coordinate system. This last transformation is required because as shown in Figure 2.8, the origins of the two coordinate systems are not typically co-located. C_x and C_y are the horizontal and vertical offset of the IMG coordinate system from the SEN coordinate system.

$$X_{IMG} = \overline{X}_{SEN} + Cx \qquad Y_{IMG} = (AR)\overline{Y}_{SEN} + Cy \tag{24}$$

Thus far, ten parameters for each camera have been presented. These parameters must be determined before an image correlation can be performed. The aspect ratio, AR, will remain constant for a given camera. As such, AR can be determined independently. The other ten parameters change with different camera locations and different lens arrangements and must be determined for each test. To calibrate the system, a number of photographs of a grid are captured with both cameras and equations 19 through 24 are used to relate the locations of points on the photos to a location in space.

III. Experimental Technique

Specimen Manufacture and Preparation

Two specimens were manufactured at the Air Force Research Laboratory Materials Directorate (AFRL/RX). The first was an aluminum bar and the second was a graphite/epoxy test coupon.

Specimen 1 Aluminum Bar.

The aluminum specimen was manufactured from a 7050-T73651 1.27 cm thick plate on a Bridgeport mill. First, a bar approximately 23 cm by 5 cm was cut from the plate. Next, the bar was milled to 20.32 cm by 3.81 cm. Each of the two long edges and two short edges were machined to ensure 90 degree corners. Both faces of the bar were then milled to reduce the thickness to 0.635 cm. Slight machining marks were left on the bar, which were subsequently removed from the face where the diffraction grating and speckle pattern were to be placed.

Figure 3.1 Aluminum Specimen

The aluminum bar was prepared for the application of the diffraction grating by wet sanding with up to 600 grit abrasive cloth. Next, a small amount of Enviro Tech pour-on epoxy was mixed to attach the diffraction grating to the specimen. The volatiles were removed by placing the un-cured epoxy in a Ladd Research Industries vacuum evaporator. A centrifuge was then used to remove solid particulates noted in the epoxy.

While the epoxy was in the vacuum evaporator, the diffraction grating was prepared for application to the specimen. The horizontal and vertical lines on the grating were found using the alignment fixture shown in Figure 3.2. The fixture allowed the diffraction grating to be rotated by very small angles. The alignment fixture was composed of a Newport 481A rotation stage mounted vertically on a Newport breadboard. The breadboard was marked with a line parallel to the plane of rotation of the rotation stage.

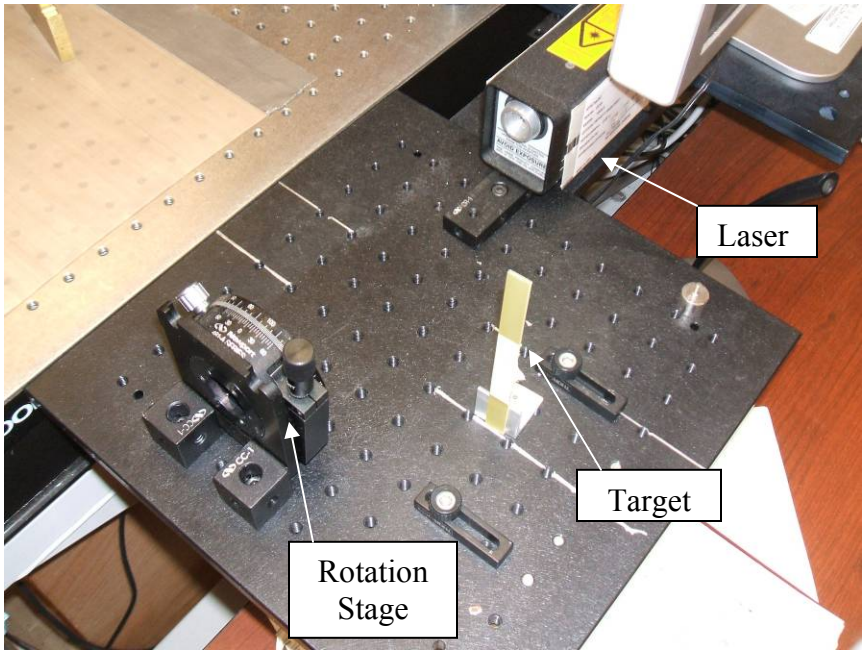

Figure 3.2 Alignment Fixture

The grating, which was delivered from the manufacturer attached to a glass plate approximately 5 cm by 5 cm, was attached to the rotation stage. Next, a Uniphase 108-0 Helium-Neon laser was directed at the grating,. The cross line diffraction grating caused the laser to split into four sub-beams, two in a horizontal plain and two in a vertical plain. A target was placed on the parallel line such that one of the two beams in the horizontal plane fell on the target. The location of the laser point was marked and the target was transferred along the line until the other horizontal beam struck the target. The location

of the second laser point on the target was compared to that of the first. The diffraction grating was then rotated until the location of the two laser points fell at the same vertical location on the target. This process ensured that the horizontal diffraction lines were parallel to the base plate of the alignment tool. An alignment shim was then bonded to the glass plate containing the diffraction grating. This shim was ensured to be parallel to the base plate of the alignment tool, and thus to the horizontal lines in the diffraction grating as well.

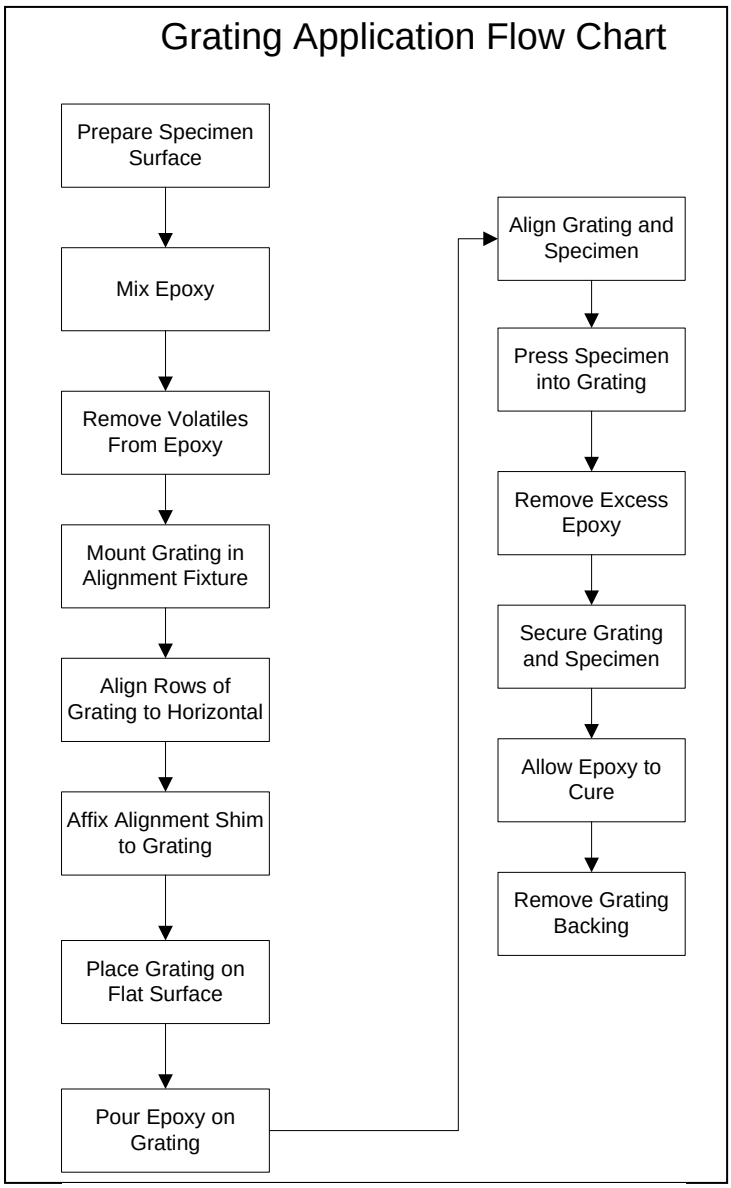

Figure 3.3 Grating Application Flow Chart

The diffraction grating was then bonded to the aluminum bar using the epoxy previously mixed. First, the glass plate containing the diffraction grating was laid on a Teflon mat, grating side up. Next, a thin line of epoxy was poured on the grating. The bar was then placed on the grating such that it floated on the epoxy. The bar was gently pushed into the epoxy until epoxy seeped from between the bar and the glass plate. The bar was then moved so it was in contact with the alignment shim. This aligned the bar and the lines in the diffraction grating. Excess epoxy was removed with cotton swabs. The bar was secured in place and the epoxy was left to cure. After the epoxy cured, the glass plate was removed by turning the bar so that the glass plate faced down. Next, the glass plate was sharply struck with the handle of a screwdriver. The glass to grating interface failed as it was much weaker than the grating to epoxy interface. The glass plate fell off, leaving the grating attached to the specimen.

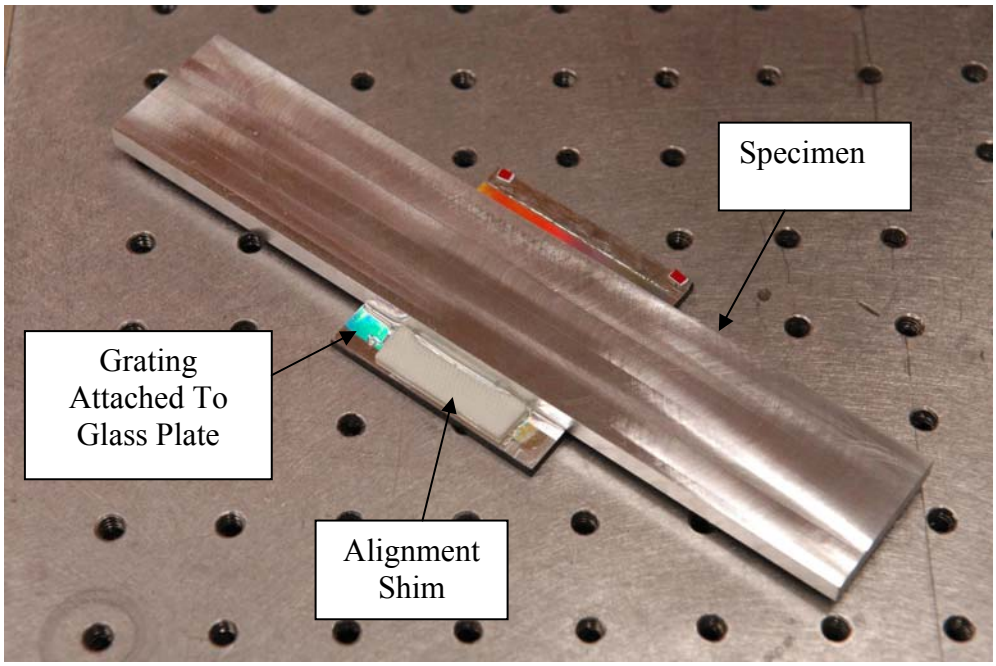

Figure 3.4 Diffraction Grating Being Bonded to the Aluminum Bar

Specimen 2 Graphite/Epoxy Coupon.

The second specimen was constructed from Cytec IM7 unidirectional carbon fiber pre-impregnated with Cytec 977-3 resin in a $[-45_2/0_2/45_2/90_2]_S$ pattern. This layup schedule was selected to cause significant inter-ply strains. Sixteen 30.5 cm by 30.5 cm squares of the unidirectional pre-impregnated carbon fiber were cut from a roll approximately 1.5 meters wide. The carbon fiber was attached to a paper backing to prevent the layers on the roll from bonding together. Eight of the squares had the fibers running parallel to the sides, and eight of the squares had the fibers running at a 45 degree angle to the sides. The first ply was laid fiber side down on a flat plate and the backing removed. The next ply was placed on top of the first and pressed down and the backing removed. The remaining 14 plies were applied in this manner and in the prescribed schedule. The panel and backing plate were then vacuum bagged and placed in an autoclave for cure as shown in Figure 3.5.

Figure 3.5 Composite Panel in Autoclave

After the panel was cured it was tested to ensure that it contained no voids or unacceptable flaws. Next, two test coupons measuring 20.32 cm by 2.54 cm panel. Diffraction gratings were then applied.

Two coupons were cut so that if one of the diffraction gratings contained excessive flaws the other could be used. The coupons were clamped together such that the edges were parallel and in the same plane. The edge of each specimen to which a diffraction grating was to be applied was lightly sanded to ensure the surface was flat and smooth. The remainder of grating application followed the same process as that used for the aluminum bar, with the exceptions that the grating was applied to the edge of the composite coupons, not the face and that one diffraction grating was large enough to cover the required area for both composite test coupons. The white rectangle in Figure 3.6 is the alignment shim. The red, yellow, green and blue areas of Figure 3.6 are the grating.

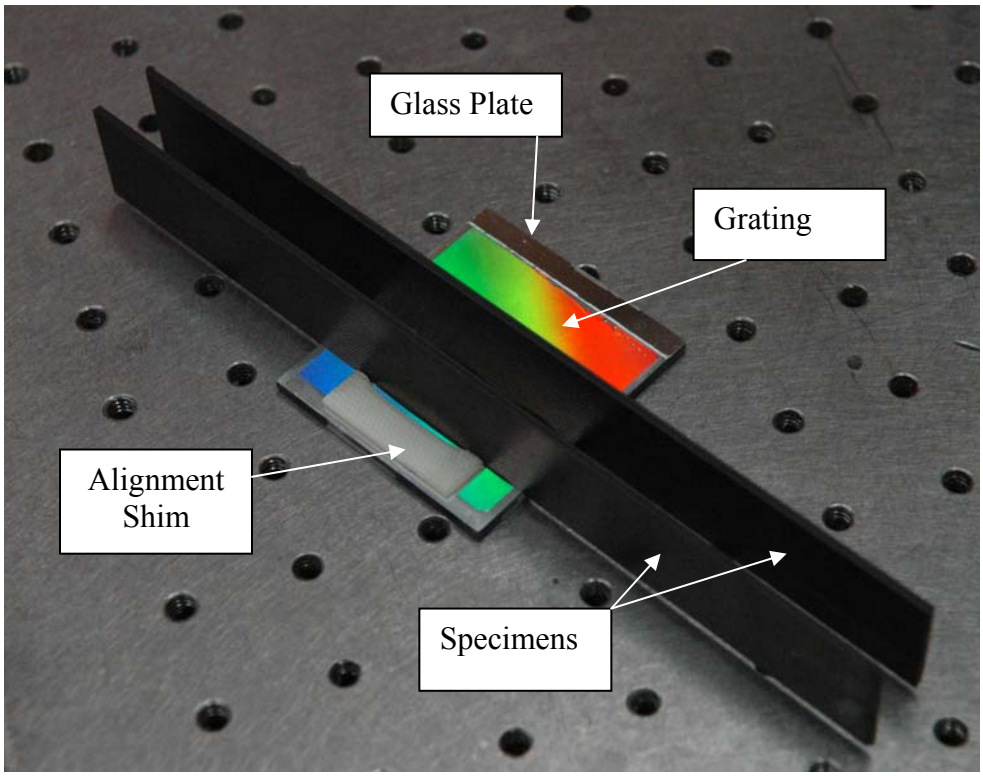

Figure 3.6 Diffraction Grating Being Bonded to Composite Coupons

Experimental Setup and Data Collection

The load frame used to apply loads to the specimens was an electrically powered, screw driven machine capable of applying a tensile load of up to 17,800 Newtons. The load frame was designed and constructed specifically for the AFRL and was not commercially available. The grips used to hold the specimens were wedge style grips which were initially tightened using a screw, but once a load was applied the wedges were pulled tighter by friction between the wedge and specimen.

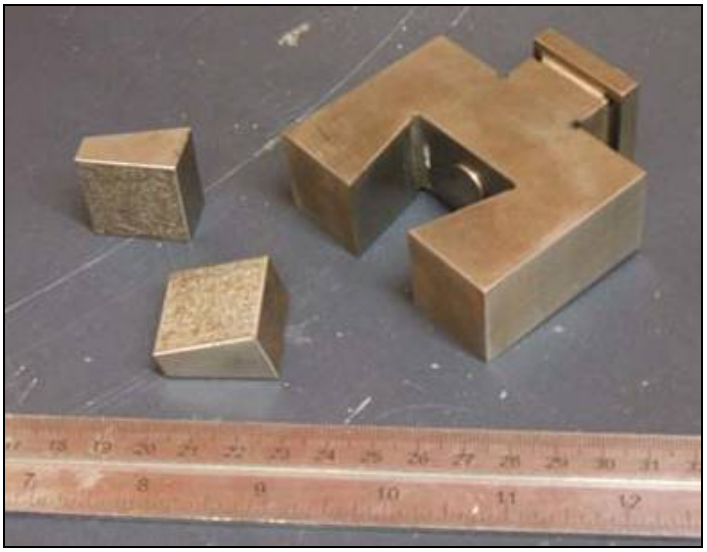

Figure 3.7 Specimen Grip and Wedge Inserts

Each specimen was first tested using moiré interferometry, then tested with DIC. Neither specimen was removed from the load frame between moiré and DIC testing. The speckle pattern was applied over the diffraction grating on the aluminum bar. More than one attempt was made to construct an acceptable speckle pattern on the composite coupon. Poor quality speckle patterns were removed using acetone. The diffraction grating on the composite coupon was destroyed by the acetone before an acceptable speckle pattern could be achieved. Thus, the speckle pattern was applied directly to the surface of the composite specimen.

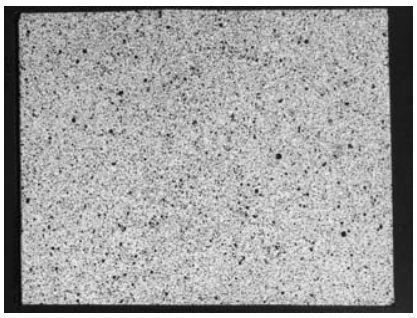

Figure 3.8a Aluminum Specimen Speckle Pattern

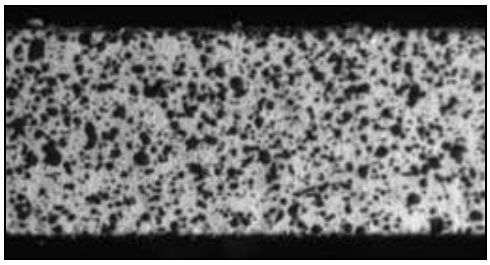

Figure 3.8b Composite Specimen Speckle Pattern

The interferometer used for the moiré portion of testing was a four beam interferometer. The light source was a single helium-neon laser with a 632.8 nm wavelength. The single laser beam was split into four beams in the interferometer, two of which were blocked while the alternate fringe pattern was captured. The wave fronts produced by the two beams used for each field exited the interferometer horizontally from a port near the top of the interferometer. The two wave fronts then traveled horizontally to a spinning etched glass pane. The two wave fronts produced the fringe patterns on this glass plate. The glass plate was spun to reduce noise caused by the texture of the plate. A black semicircular shroud was placed around the glass plate to reduce extraneous light from the interferogram. A 2 mega-pixel camera was used to capture digital photographs of the fringe patterns on the glass plate. The same moiré hardware and arrangement was used for both specimens.

The phase data were extracted from the fringes using a program called Superfringe. This software was written by David Mollenhauer. Displacement fields were constructed and analyzed using Fortner Transform PPC for Macintosh computers. The operating system that Fortner Transform was designed for use with was OS 9.2.

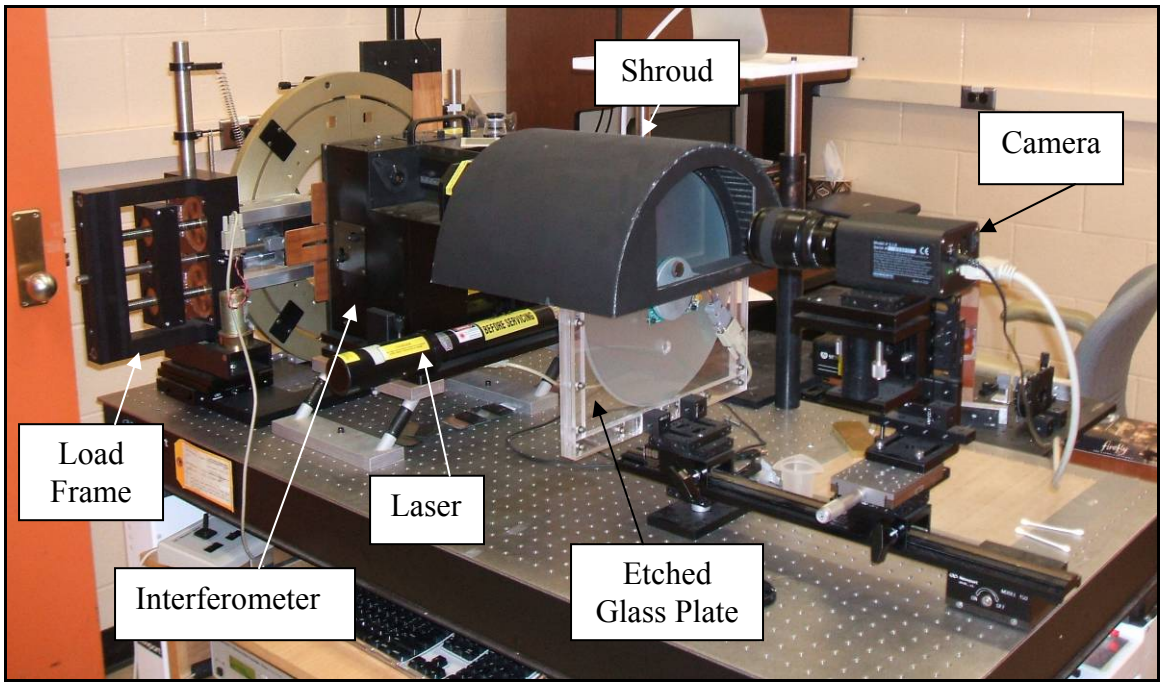

Figure 3.9 Moiré Interferometry Apparatus

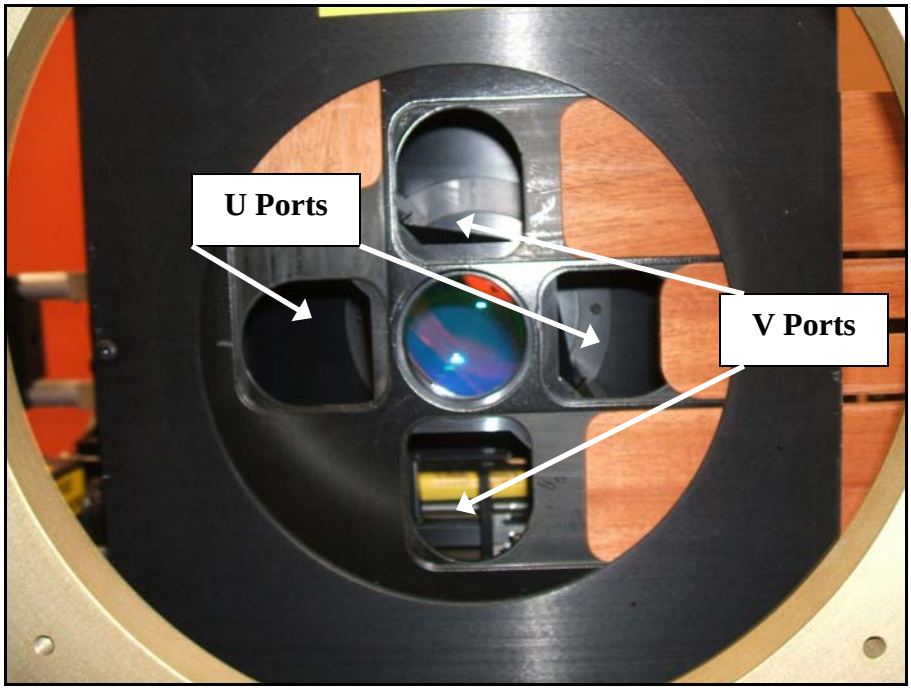

Figure 3.10 Front of Moiré Interferometer

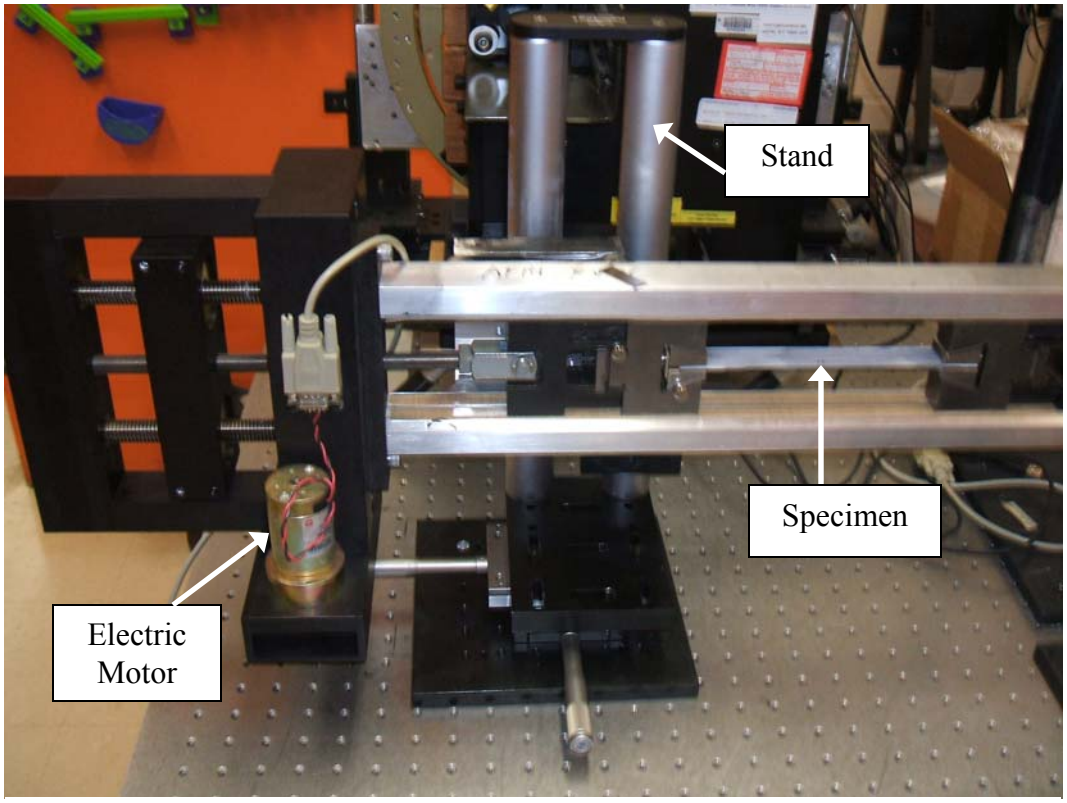

Figure 3.11 Load Frame

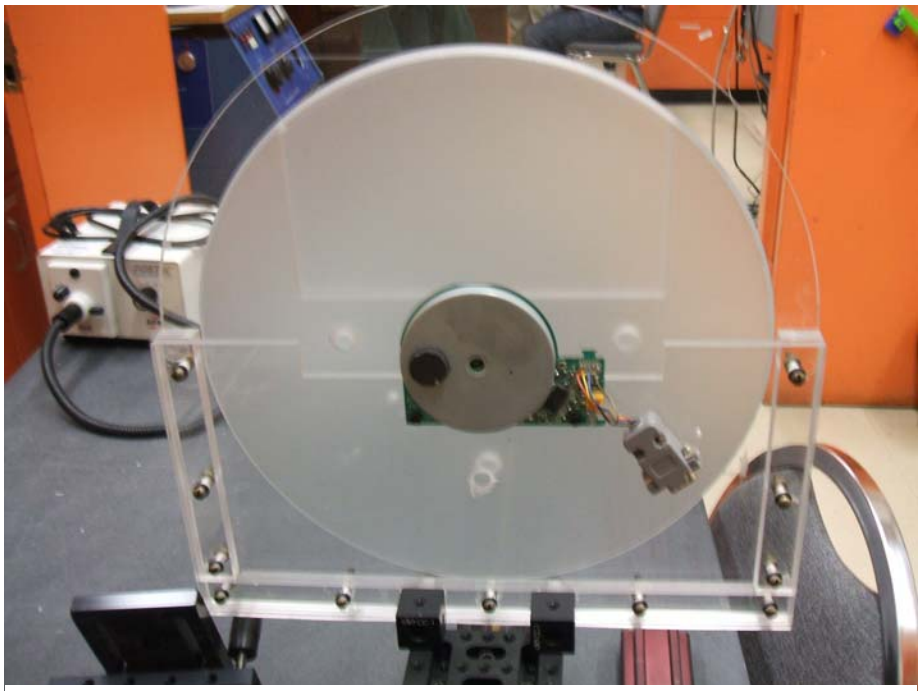

Figure 3.12 Etched Glass Pane

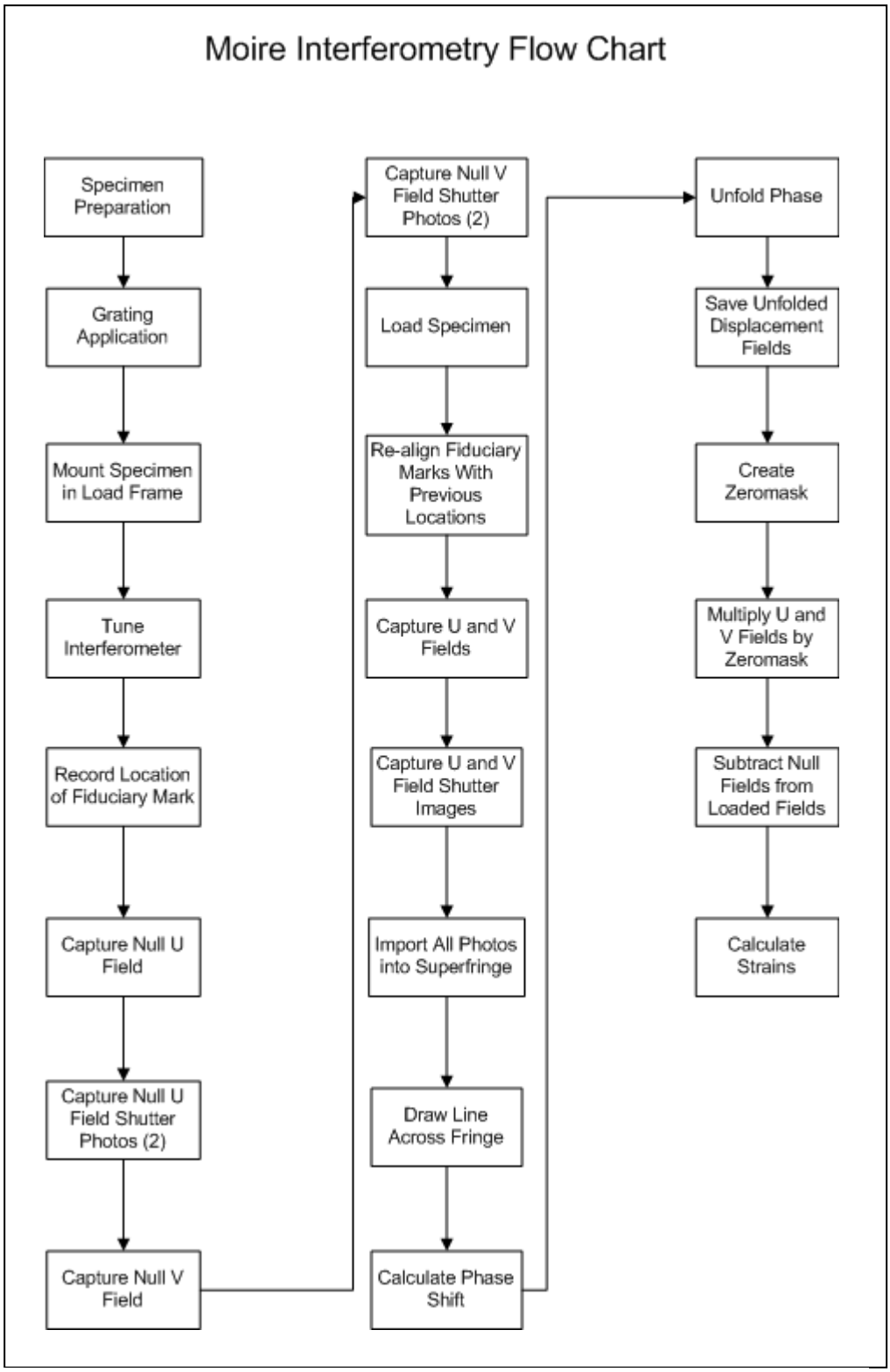

Figure 3.13 Moiré Interferometry Flow Chart

The same load frame was used for DIC testing as was used for moiré testing; however, it was moved to allow room for the camera arrangement. The aluminum bar was tested using the cameras supplied with Vic-3D 2006, Dolphin F201B's. Testing took place in the Photomechanics Laboratory of the AFRL. One of the Dolphin cameras failed between testing of the aluminum bar and testing of the composite coupon. No replacement was available, so other cameras were used for the composite coupon testing. Testing of the composite specimen took place at the Air Force Institute of Technology (AFIT) using CCD 1300BG cameras supplied by Trilion Systems for a competing DIC system. System calibration photographs and specimen photographs of the composite specimen taken at AFIT were loaded into and analyzed using Vic-3D 2006 at the AFRL Photomechanics Laboratory.

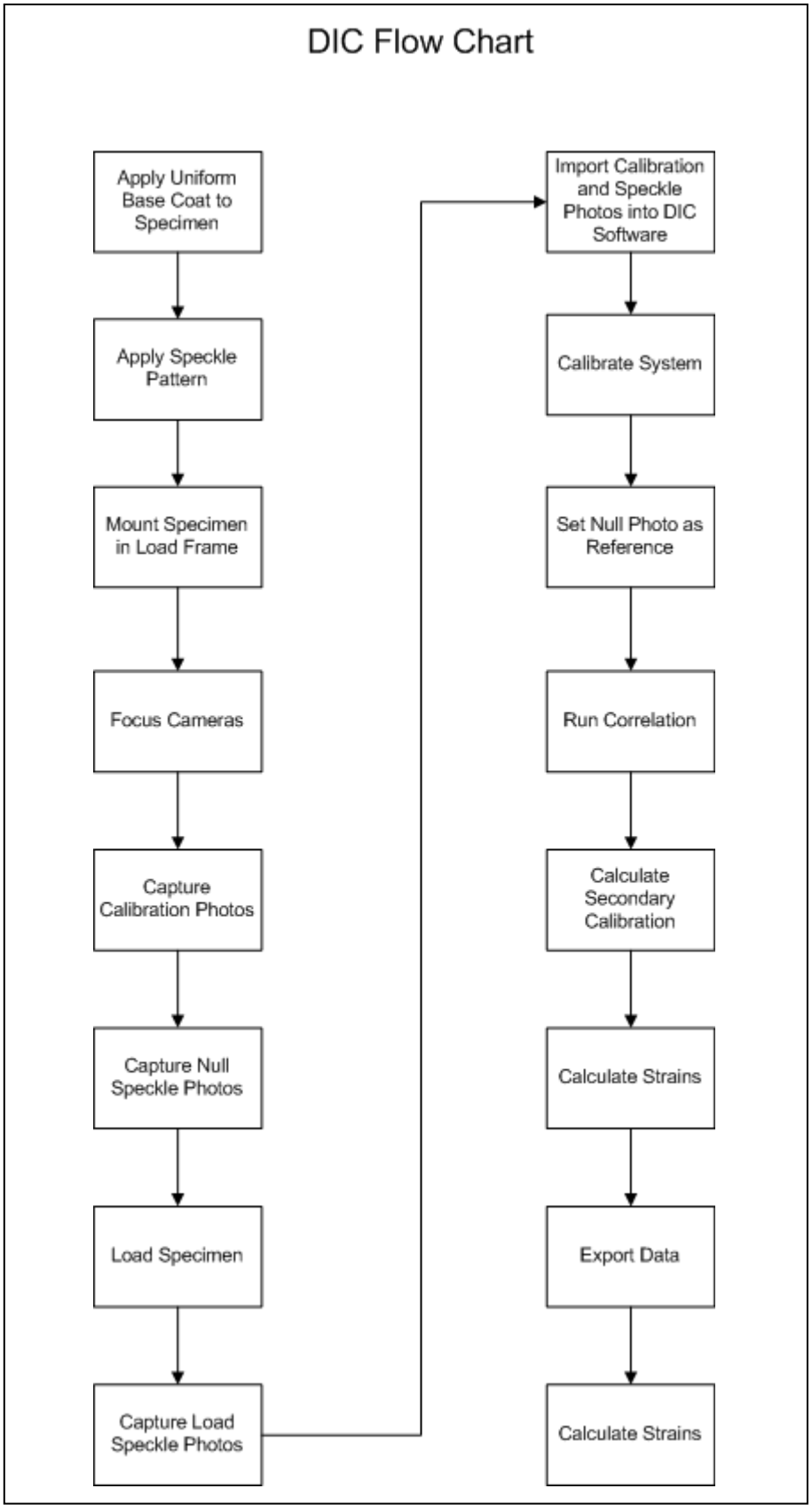

Figure 3.14 DIC Flow Chart

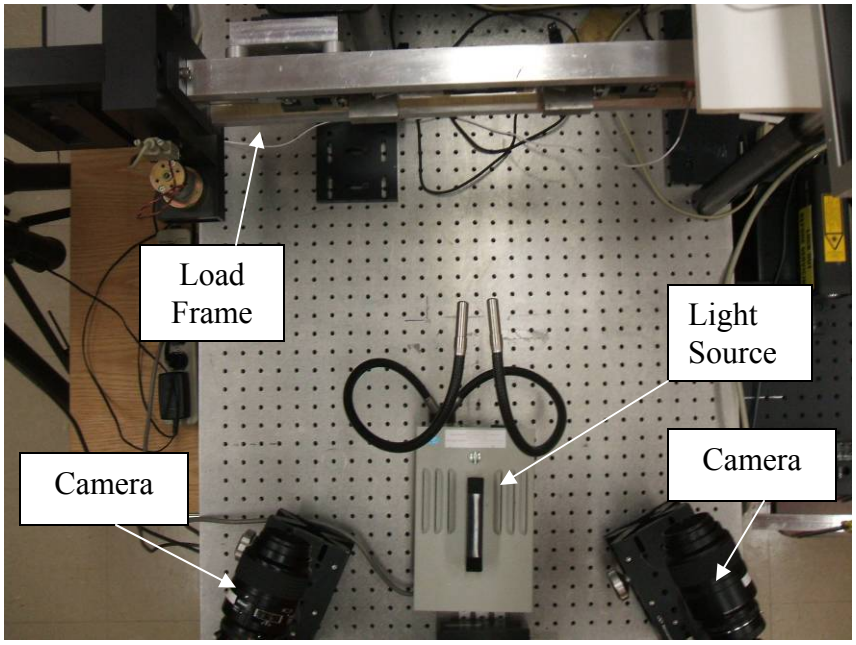

Figure 3.15 DIC Apparatus at AFRL

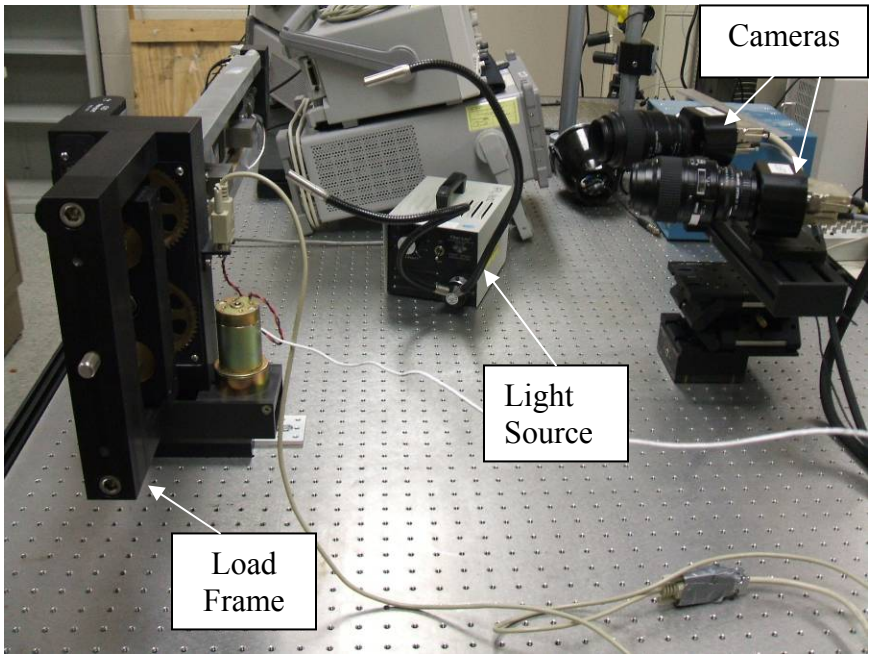

Figure 3.16 DIC Apparatus at AFIT

Aluminum Bar – Moiré Interferometry.

The first specimen tested was the aluminum bar. The bar was mounted in the grips and the grips were tightened to retain specimen position during placement in the load

frame. After the specimen and grips were attached to the load frame, the load frame was rotated about an axis normal to and running roughly through the center of the diffraction grating. This rotation aligned the specimen and interferometer such that the horizontal furrows of the specimen grating would align with the horizontal rows of the virtual grating. Next, the interferometer was tuned such that the two wave fronts produced by the interferometer fell in the same location on the spinning glass plate.

Once the specimen was installed in the load frame and the interferometer was tuned, two photos were taken of the interferogram. The first photo was of the specimen unloaded. The second photo was of the unloaded specimen interferogram, but with a rigid body translation of 5 mm. This series of photos was used to determine the scale of the photographs of the unloaded specimen, and determine alignment of the specimen after loading. Next, six photographs of the no load U field fringe patterns were captured while a current was applied to the heated wire coils on the base of the interferometer. The current heated the legs of the interferometer base plate, causing the interferometer to shift, inducing a phase shift in the interferogram. The current was removed from the coils and two photographs of the specimen were taken: one with one U field beam blocked, one with the other U field beam blocked. The V field beams were unblocked (U field beams were blocked) and another series of photos were taken of the no load fringe pattern with current applied to the coils. The current was removed and two photographs were captured of the specimen, one with one V field beam blocked, one with the other V field beam blocked. The process was repeated for loads of 4,450 N, 8,896 N and 17,328 N. Between each loading; except for the 4,450 N load, the specimen was translated to position fiduciary marks on the grating in the same location they were in prior to loading.

The realignment was not performed for the 4,450 N load condition. The lack of alignment for the 4,450 N load condition caused some extra work during analysis to properly align the fiduciary marks on the specimen. This did not induce any inaccuracy into the test results as the alignment was performed during the analysis. Also, after each loading the specimen was rotated to remove fringes caused by rigid body rotations induced during the load change. Rigid body rotations were determined to be present because the fringe pattern was slanted at a different angle after loading as opposed to before loading. Had no rotation occurred the fringes would have the same orientation.

Aluminum Bar – Digital Image Correlation.

After moiré data had been taken for the aluminum bar, the load frame was removed from its stand, and the speckle pattern was applied as discussed earlier. The load frame was then positioned away from the interferometer to provide room for the image correlation setup. The cameras were mounted approximately 46 cm from the specimen with a separation of approximately 41 cm between the cameras. The cameras were mounted on Newport 271 optical jacks, which were mounted on Newport 150 magnetic bases. A Fetherlite Series 180 fiber optic light source provided illumination for the test. Each camera was fitted with a Nikon AF Micro Nikkor 105 mm lens. The Area of Interest (AOI) on the specimen was surrounded by a piece of non-reflective black paper. This paper framed the AOI with distinct boundaries allowing the specimen to be imaged through the cameras such that the entire AOI was present but very little margin surrounded the specimen in the images.

The first step of the DIC test was collection of system calibration photos. 18 photos of a calibration target were taken with each camera. The target used was a square piece

of glass with a 9 by 9 grid of white dots with 3 mm spacing on a black background. Three of the dots were actually rings with black centers. It was critical for all three rings to appear in each photograph used in calibration. If all three were not visible, then Vic-3D 2006 would not use that photograph in the calibration sequence. The target was placed on the load frame in front of the AOI and photographs were captured with the target in various placements. After the calibration photographs were taken, the target was removed and the load frame repositioned so the specimen would be located in the same area as the calibration target had been. Two photographs were taken of the speckle pattern with each camera for each load condition: 31, 4450, 8896, and 17328 N. Only one photograph from each camera for each load condition would be analyzed, the other was taken to use in case a problem was found with one of the other photographs.

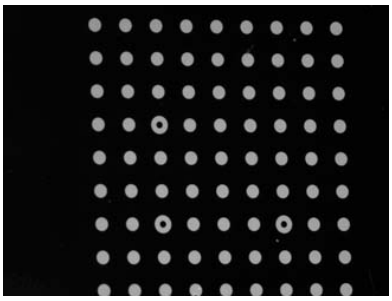

Figure 3.17 9 X 9 Calibration Target With 3 mm Spacing

The calibration photos were imported into Vic-3D 2006 and the calibration function started. First, the auto-threshold option was disabled and the threshold value adjusted for the first photo until all dots and rings were clear and sharply defined. Then the automatic point extraction routine was run. This routine found the centers of most of the dots and rings for use in the determination the parameters needed for the camera model and definition within the DIC program of the camera layout. Threshold values of photos unextracted during the first pass were adjusted and the automatic extraction was run

again. After the second pass, threshold values were adjusted and the manual extraction button selected for remaining unextracted photos. A possible synchronization error was noted during calibration. A previous discussion with technical support from Correlated Solutions; the manufacturer of Vic-3D 2006, caused the author to expect this error message and determine that it was not an issue because of the extremely sensitive threshold for the trigger of this warning message.

After calibration, the 31 N load pictures were set as the reference images and an AOI was set that was as large as possible but allowed the entire area to be visible in all photographs. A seed point was placed near the right side of the AOI near the vertical centerline, and the location input into the program for each photograph of the different loads. The seed point gave the program a point at which to start the correlation. The placement of the seed point was not required; however, it sped up the correlation process. Separate correlations were performed for five subset sizes (11, 25, 51, 75 and 100 pixels) and five step sizes (5, 15, 25, 40 and 50 pixels). The five pixel step size was the only step size looked at for the 11 pixel subset because of excessive data dropout seen with the other step sizes. A secondary calibration was performed after each correlation. This secondary calibration used the speckle pattern in each of the photographs to refine the calibration. The strains were then calculated. Last, the data generated were exported to Comma Separated Value (CSV) files. Exported data included X, Y and Z locations; U, V and W displacement data; and strains.

Graphite/Epoxy Specimen – Moiré Interferometry.

With the exceptions listed below, the same process was followed for the moiré interferometry testing of the composite specimen as for the aluminum bar. The specimen

and grips were placed in the load frame such that the edge of the specimen was presented to the interferometer. This edge displayed all sixteen plies. The edge was analyzed because the fiber orientations in the different plies caused significant inter-ply strains. The second difference in the process was that a carrier of rotation was included in the null field fringe patterns to ensure sufficient fringes would be present in the loaded conditions for analysis. The carrier was induced by rotating the specimen. The carrier fringes in the U field were horizontal and the carrier fringes in the V field were vertical. The induced fringe pattern was not removed when the specimen was loaded. The carrier of rotation would not effect the results of the experiment because the carrier fringe was included in both the null fringe and the loaded fringe patterns. In an attempt to reduce visco-elastic effects the specimen was tested at only three loads: 445 N (considered the null load), 9,345 N, and again at 445 N. Lastly, the specimen was not translated to capture a scale. The scale was instead determined by dividing the specimen thickness by the number of pixels in the in the thickness of the specimen in the photographs.

Graphite Epoxy Coupon - Digital Image Correlation.

Although attempts were made to test the composite coupon similarly to the aluminum bar with respect to DIC, significant differences between the two tests did occur. As stated earlier, the cameras used for the composite coupon were different than those used for the aluminum bar. Not only were they made by different manufacturers, but the replacement cameras were of lower resolution (1.3 mega-pixel for the composite coupon vs. 2 mega-pixel for the aluminum bar). Similar optics were used however. The same Nikon Micro Nikkor 105 mm lenses were used. Two Nikon Teleconverter TC-201 2X lens extensions were used on each camera to achieve the higher magnification required.

The specimen grating was also removed from the specimen before an acceptable speckle pattern could be achieved. The grating did not effect the quality of the speckle pattern, it was merely destroyed during repeated application and removal of unacceptable speckle patterns. The location of the test was also different between the two tests.

After the load frame was moved to AFIT the cameras were set up and the speckle pattern applied to the specimen. Thirty-one calibration photographs were taken with each camera of the calibration target. The target was a 9 by 9 dot grid with 0.5 mm spacing. As with the aluminum bar, the load frame was moved away from the cameras far enough to allow the calibration target to be placed in the same location the edge of the specimen would be at during the test. After the calibration photos were taken, the load frame was repositioned to place the specimen in the same location the target had been. Two photographs were taken with each camera of the specimen at a load of 445 N, these were used as the reference photos. The specimen was then loaded to 9345 N, and two photos were taken with each camera. The load on the specimen was then reduced to 445 N and two additional photos were taken with each camera. Only two of the photos; one from each camera, were used for each loading case. The other two were reserved for use in the event the first two were unusable.

The calibration photos and the photos of the loaded specimen were taken back to the AFRL laboratory for processing in Vic-3D 2006. First, the photographs were loaded onto the computer, then the camera calibration routine was started. The automatic threshold was turned off, and the threshold value was adjusted until the center points of the dots and circles of the calibration target were extracted. The system was then calibrated. After calibration, the first 445 N load case photographs were set as the

reference photographs. An AOI was defined which covered all but the edges of the specimen photograph, and a seed point was inserted. Next, a correlation was run for twelve subset size and step size cases. Subset sizes included 25, 50, 75 and 100 pixels; step sizes included 10, 25 and 50 pixels. The 25 pixel subset with 50 pixel spacing case was not saved due excessive data dropout. After each correlation a secondary calibration was performed to increase the accuracy of the correlation. The strains were calculated for that correlation and then the data was exported to CSV files before the next correlation was run with changed subset or step size.

Data Conditioning

The raw data from moiré tests were digital photographs in a Tagged Image Format File (TIFF). Numerous steps were required to extract strain fields from the photographs of the specimens. Vic-3D 2006 produced CSV files containing X, Y and Z locations, U, V and W displacements and strains. While the DIC output files contained strain data, the strains were recalculated from the U and V displacement data using the same process as was used for the displacement fields produced with moiré data. The recalculation of strains was performed solely for the sake of the comparison between the two methods.

Aluminum Bar - Moiré Data.

The first step of conditioning the moiré interferometry data was to import them into Superfringe. Once all six interferograms, and two shuttered images were imported into Superfringe, the folded phase was analyzed. The folded phase analysis started with drawing a line across one full fringe. The phase shifts along this line were compared to the ideal case. If the phase data did not closely match the ideal, a new line was selected and compared again. The next step was to pick a point in the fringe pattern at which the

unfolding was to begin. The software unfolded the phase, and output a displacement field. The displacement field was checked for any periodic noise patterns. Once the displacement field was determined to be acceptable, the file was saved. This process was repeated for the U and V field for each load case.

After the displacement fields were exported from Superfringe they were imported into Fortner Transform PPC. The files were copied and saved under a different name to protect the raw displacement data. The displacement files for the 4450 N load case were synchronized with the other displacement files. This was done because the specimen had not been realigned with the null position after loading. The portion of the data that was present in all displacement fields was then extracted and saved to a new file. A scaling factor was determined which converted pixel location to millimeters. As it turned out each pixel constituted a distance of 0.021 mm. The data was scaled and the coordinate system was oriented such that the vertical positive was down. The *zeromask* shown in Figure 3.18 was then created to remove areas with corrupted data in any of the fringe fields from all displacement fields. The *zeromask* was created by making a new array for each displacement field that was the same size as the displacement field which had a value of one in each element that the displacement field had a nonzero value. Any location in the *zeromask* that corresponded to a zero value in the displacement field was set to zero. The red area, which comprises the majority of Figure 3.18, represents the elements with values of one. The small black areas of the figure represent elements with values of zero. The *zeromasks* for all loading cases for both the U and V fields were multiplied together to create the master *zeromask*. The master zeromask was multiplied by the U and V fields for each load case (including the null fields). Last, the U and V

null fields were subtracted from the U and V fields of each load case to remove the null fringe data.

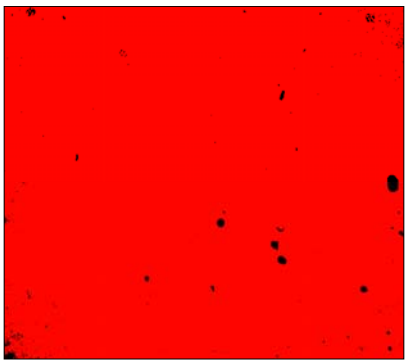

Figure 3.18 Zeromask for Aluminum Bar Moiré Interferometry Data

Aluminum Bar - Digital Image Correlation Data.

The CSV files generated by Vic-3D were loaded onto a Macintosh computer and opened with Fortner Transform PPC. The columns containing U, V and W displacements for each data point were extracted and saved to separate files. This produced a file for each of the three displacement fields from each subset size and step size combination. The format of the data in these files was a table format indexed by X and Y pixel location. The index of each file was then scaled so the displacement fields would be displayed in millimeters instead of pixel location, and the coordinate system was relocated to the left side centered vertically. Additionally the vertical axis was positive down. Next, the strains ε_x, ε_y and γ_{xy} were calculated using equation 6 from Chapter 2.

Graphite/Epoxy Coupon - Moiré Data.

The fringe patterns for the composite coupon were loaded into Superfringe and analyzed similarly as the fringe patterns for the aluminum specimen. As before, Superfringe produced displacement fields. The displacement fields for the null (445 N)

and 9345 N load cases were loaded into Fortner Transform PPC. First the top and bottom of the displacement fields were cropped because they were not horizontal and also because the top and bottom rows of data were jagged due to the edge of the specimen. Next, the left edge was cropped because a large flaw in the diffraction grating corrupted the data in that area. Next, remaining areas of the cropped displacement fields with data dropout were filled. The areas that were filled were very small, five to ten pixels in diameter. The scheme used to fill the missing data was a linear interpolation which used data from all sides of the void to reconstruct the missing data. The U and V null fields were then subtracted from the U and V fields for the 9345 N load case. The optics used in the moiré data collection had flipped the image vertically, so the data was again flipped using the rowflip macro. Last, the data was scaled to convert the location of each pixel into millimeter format. The scaling also oriented the coordinate system such that the horizontal axis was located on the centerline of the specimen, and the vertical axis was at the left edge of the data. The vertical axis was positive down. The original axis system was oriented with the origin at the top left corner with the positive horizontal direction in the right direction, and the positive vertical direction down. Figure 3.19a depicts the original axis system and Figure 3.19b depicts the new axis system.

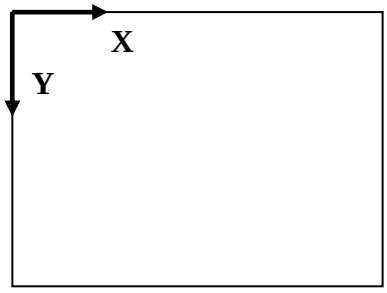

Figure 3.19a Original Axis System

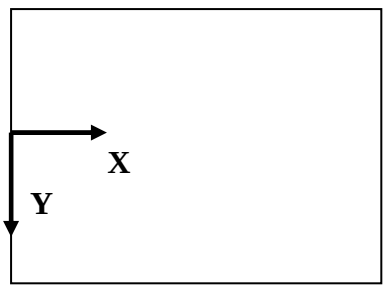

Figure 3.19b New Axis System

Graphite/Epoxy Coupon - Digital Image Correlation Data.

The CSV files for the composite coupon were loaded onto the Macintosh computer, then U, V and W displacement fields were extracted and saved to individual files. However, since DIC automatically subtracts the reference field (the equivalent to the null field for moiré) only the CSV files for the 9345 N load case were processed. Next the fields were scaled so they were indexed in mm. The coordinate system was set to be located at the extreme left edge of the AOI and the vertical centerline of the specimen. Again, the coordinate system had the vertical axis positive down. The vertical centerline was found by computing γ_{xy} (for the unscaled data set) and then taking a vertical line graph and determining the location where the shear strain crossed through zero. For this specimen the shear strain was expected to change signs at the centerline. After the coordinate system was placed and the indices were scaled ε_x, ε_y, and γ_{xy} were found using equation 6 from Chapter 2.

Data Analysis

Because the signal to noise ratio in the data was the best, only the 17,328 N load was analyzed for the aluminum bar.

Aluminum Bar.

The moiré data was resampled to give the same resolution as that of the displacement fields for each DIC subset size and step size. Four imperfections on the diffraction grating which were visible in the moiré data were also visible in the Z location DIC data. Thus, the two data sets were overlaid and the photos cropped so that the data tables underlying the photographs were of the same size, and each element of both moiré and DIC data referred to the same location on the specimen. This allowed a direct

comparison between the two methods at each point in the fields of view. The means of the axial strain field were calculated and compared. The primary basis of comparison was the magnitude of the axial strain. The noise in the data was a secondary point of comparison.

Graphite/Epoxy Coupon.

Unlike the data for the aluminum bar, the strains calculated from the moiré data for the composite coupon were not resampled. The ply orientation of the specimen was chosen to cause rapid changes in strain and strain gradient. The intention for this specimen was to determine the spatial resolution capability of DIC. Resampling the data would have degraded the changes in strain and strain gradient produced by the moiré data. The strains measured with moiré interferometry were smoothed to reduce noise. Each data point was averaged with the eight surrounding data points. This averaging was performed 25 times. After smoothing, a line graph was taken of ε_y and γ_{xy} for a vertical slice through the specimen. Similar vertical line graphs were taken from each DIC subset size/step size combination. The two line graphs were overlaid and compared for similarities.

IV. Discussion and Results

Aluminum Bar

The analysis of the data produced from the testing of the aluminum bar revealed trends attributable to both subset size and step size. The subset effects seemed to have a greater impact on the strain field than the step size. Average axial strains found from the data for both methods were compared to the theoretical strain for an isotropic material subjected to a known load to show the accuracy of each method when applied to a simple strain field. It was quite surprising that both moiré interferometry and DIC underestimated the axial strain when compared to the theoretical solution. A finite elements model is presented to support the assertion that the discrepancy was caused by the specimen slipping in the grips during the test.

Differences from Theoretical Solution.

The average axial strains were calculated for both moiré interferometry data and DIC data as discussed in Chapter 3. Both methods provided very consistent values for the mean of the axial strains, irrespective of subset size or subset spacing for DIC, or resample rate for moiré interferometry. However, when the strains from the two methods were compared, a discrepancy between the two methods prompted the calculation of the theoretical prediction of the strain. The theoretical axial strain (ε_x) was calculated using the following equation: $\varepsilon_x=P/(A*E)$, where P was the induced load, A was the cross sectional area and E was Young's Modulus. Figure 4.1 shows the mean of the strains calculated from both experimental methods and the theoretical value for the strain.

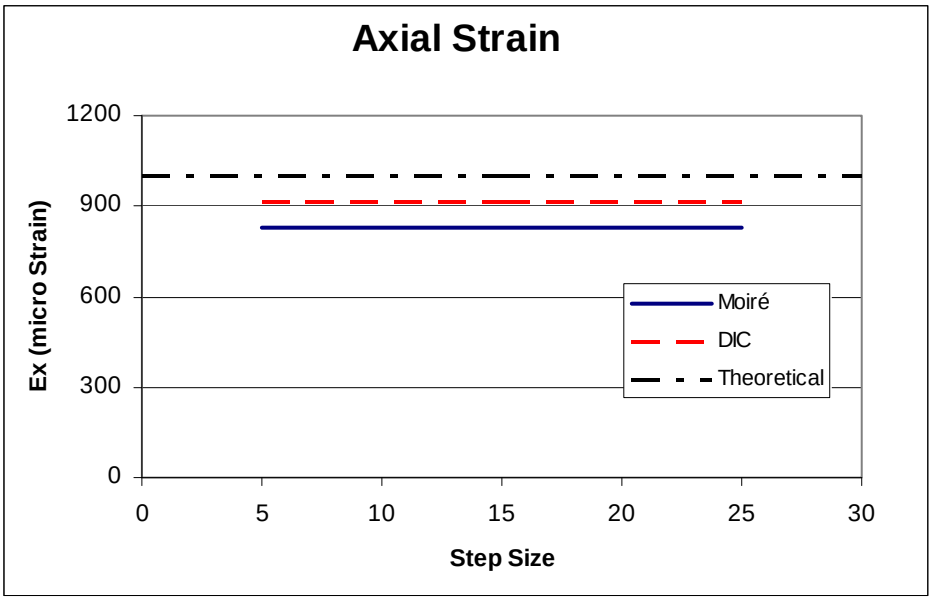

Figure 4.1 Aluminum Bar Axial Strains

The most obvious cause for the discrepancy was a faulty reading from the load cell. This theory was ruled out by checking the calibration of the load cell. It was shown to measure the load applied to the specimen within .3% at the upper range of the load frame.

The next theory to explain the discrepancy was that the specimen had slipped in the grips between the times that the null and the loaded data were taken. An uneven load imparted by the grips would induce bending capable of causing the discrepancy. This theory was supported by the fact that during loading, the display on the load cell indicated load drops. A Solid Works finite elements model was developed using the specimen geometry and material. Boundary conditions of the model are located in Table 4.1. The model represented the right half of the specimen and used a plane of symmetry to represent the left half. A solid mesh was used which contained 80,952 elements with each element 0.127 cm on each side. A total of 119,697 nodes were used at the junction of the elements. The model was subjected to a 17,328 N distributed load applied to the end of the bar.

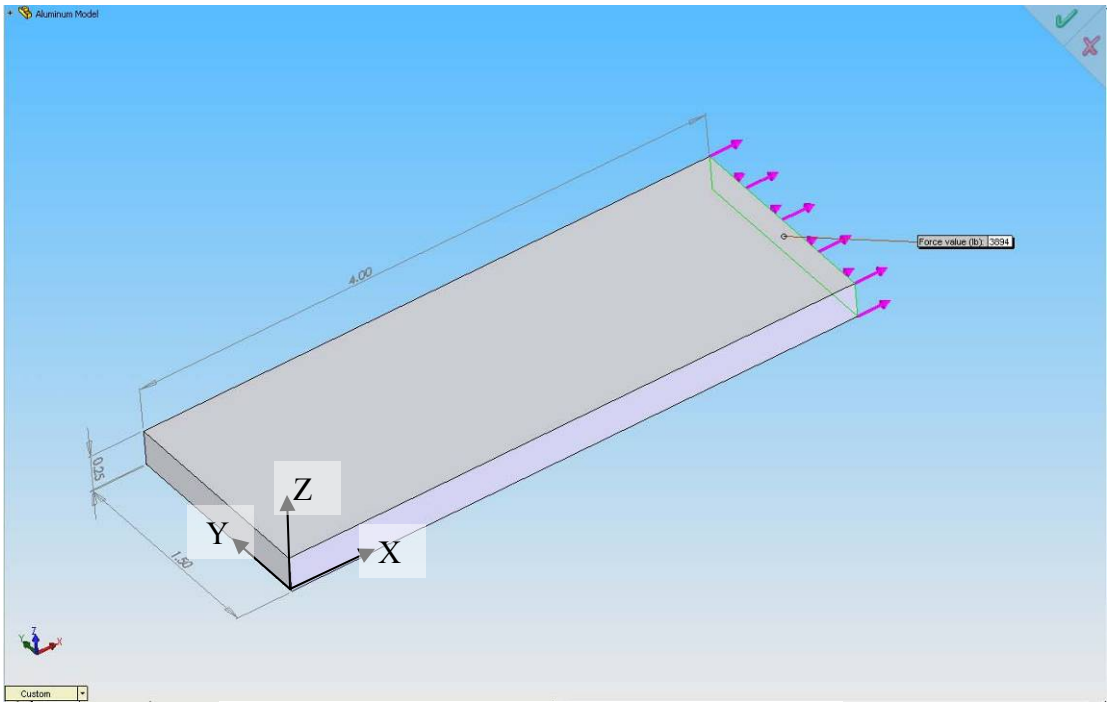

Figure 4.2 Solid Works Model of Aluminum Bar

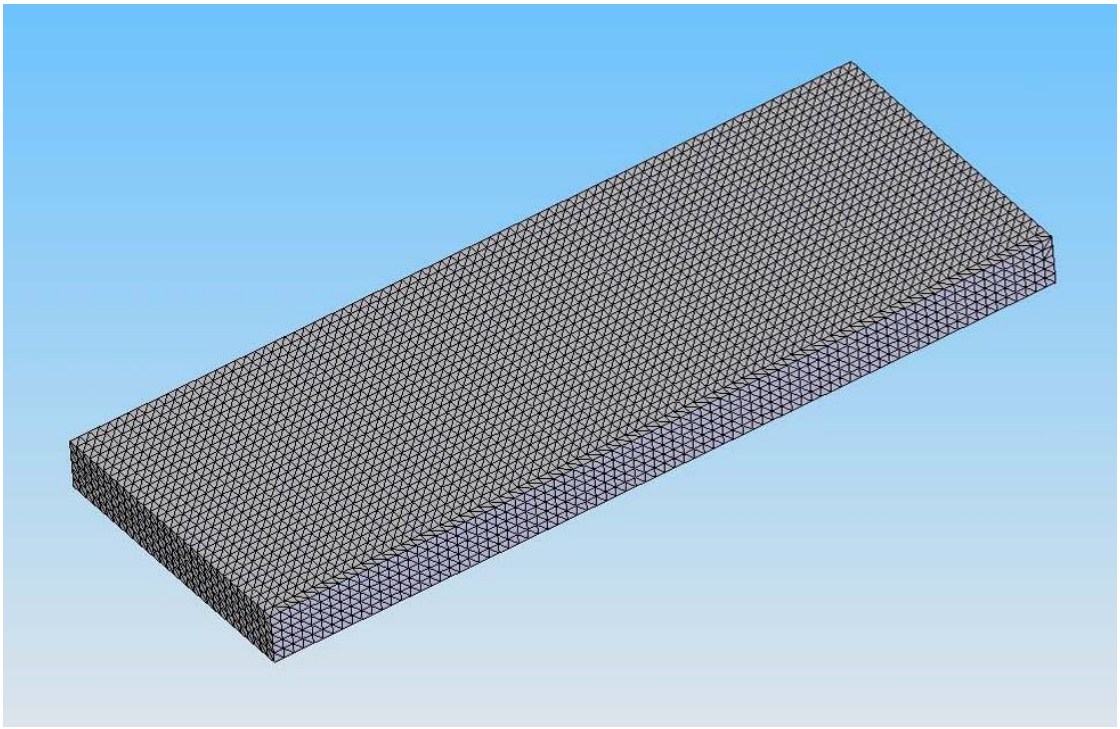

Figure 4.3 Solid Works Model Mesh

Table 4.1 Solid Works Boundary Conditions And Loads

Boundary Condition	Location of Application
U = 0	X = 0
V = 0	X = 4
Z = 0	X = 0; Y = 0
F_1 = 17,328 N	X = 4 (Distributed along the Face)
F_2 = -900 N	X = 4, Z = 0.25, $0 \leq Y \leq 1.5$ (Distributed Along Edge)
F_3 = 900 N	X = 4, Z = 0, $0 \leq Y \leq 1.5$ (Distributed Along Edge)

Grip slippage was replicated by an equal, but opposite force applied along the top and bottom edges of the right end of the bar. These two forces created a couple which would induce bending into the specimen. It was found that as little as a 900 N differential between the frictional forces produced at the grip/specimen interface would reduce the measured strain by similar amounts as the discrepancy. Furthermore, the out-of-plane displacement field produced by the Solid Works model matched very closely the displacement field produced by the DIC measurements, as seen in Figures 4.4 and 4.5. Note the curve of the regions of displacement. Marks left by the grips on the surface of the specimen as seen in Figure 4.6 further support this theory. Figure 4.6 shows direct evidence that at least some slipping of the grips occurred. Additionally, the grips were expected to have slipped less with each successive loading cycle. The moiré test was performed before the DIC test and the strains produced by the moiré measured displacements were lower than those of the DIC strains. As shown in Figure 4.1 above,

the discrepancy between the moiré data and the theoretical solution is greater than the difference between the DIC data and theoretical solution.

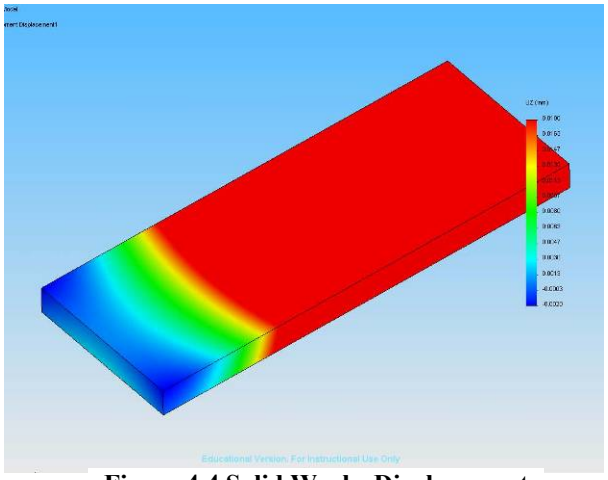

Figure 4.4 Solid Works Displacement Field for Right Half of Aluminum Bar

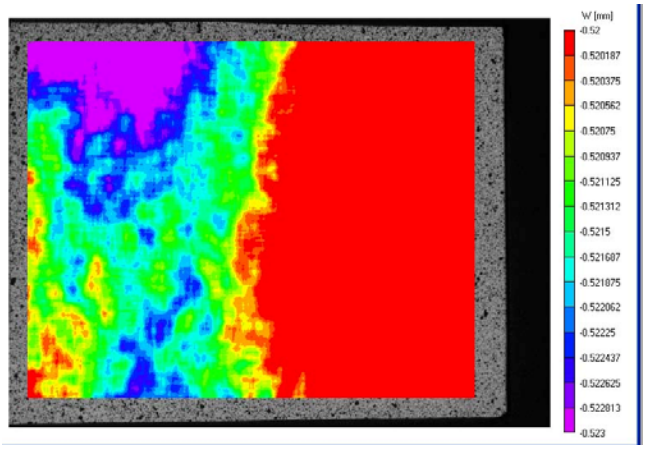

Figure 4.5 DIC Displacement Field

Figure 4.6 Marks on Aluminum Bar Produced by Slipping Grips

Subset Size Effects.

The most apparent effect of subset size on the data generated by DIC for the aluminum bar was a smoothing effect as the subset size increased. This smoothing was seen in both the displacement fields (shown in Figure 4.7) and the strain fields (shown in Figure 4.8). The rows in both figures hold the subset size constant, and the columns in both figures hold the step size constant. For the displacement fields this smoothing had the effect of making the fringes more clearly defined. For the strain fields, the smoothing had the effect of reducing the scatter present in the data. As discussed earlier, the mean of the strains produced by DIC were the very close to the theoretical strains if a margin is included for the grip slippage. However, large variations in the strains can be seen in Figure 4.8. The strain variations take an almost randomly scattered noise pattern in the fields produced with small subset sizes. The variations seemed to coalesce into large grain like structures in the strain fields produced with larger subset sizes. The strain field should have been uniform since the specimen was constructed from an isotropic material and the AOI was well away from the point of load application. The uniform strain field was substantiated by the moiré data where the strains calculated were very closely scattered about the mean, and the systematic variation in the strain field was likely caused by bending. Thus, for an isotropic material it may be better to use a small subset size, and accept the strain variations as noise.

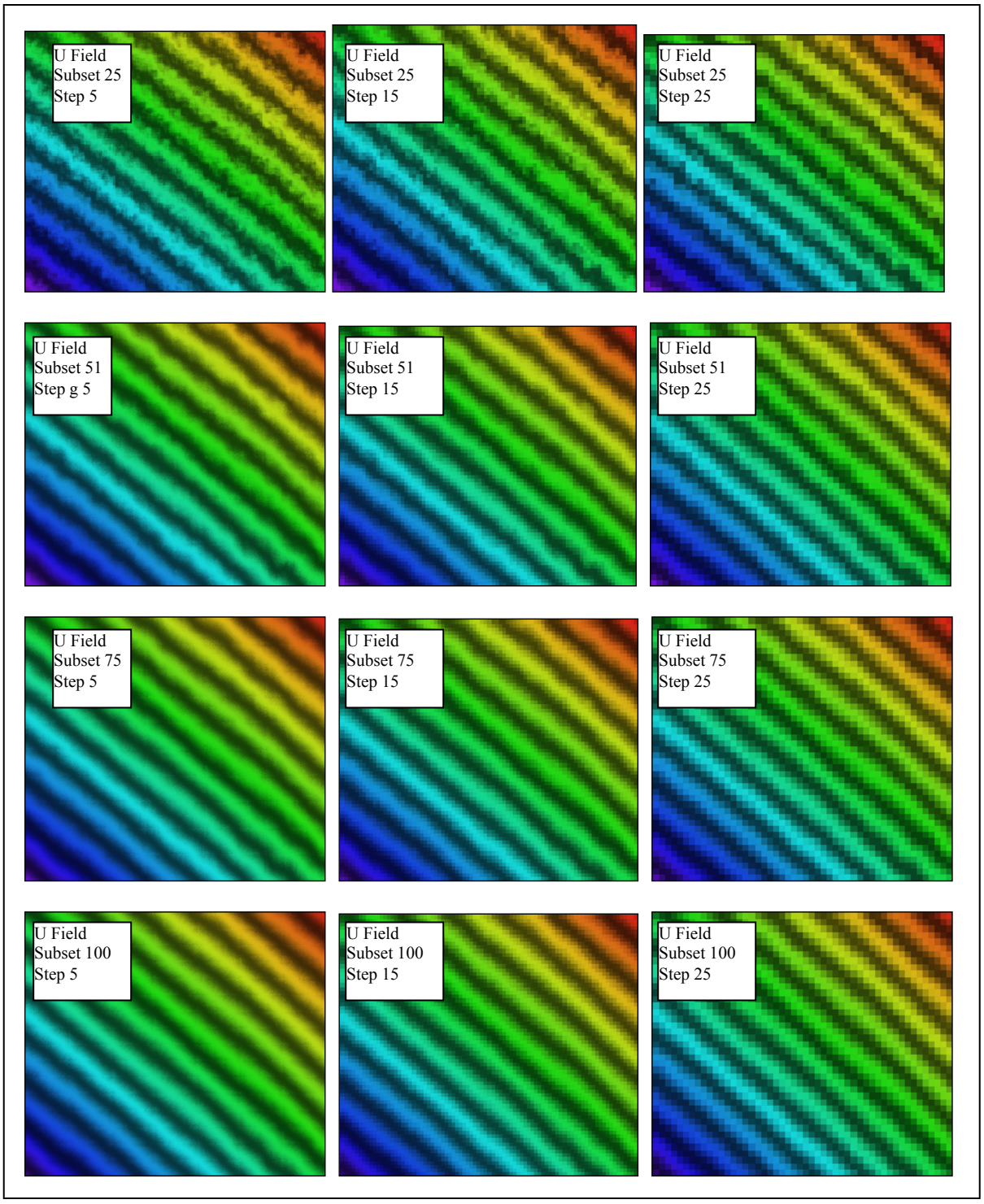

Figure 4.7 U Displacement Fields: Aluminum Bar DIC

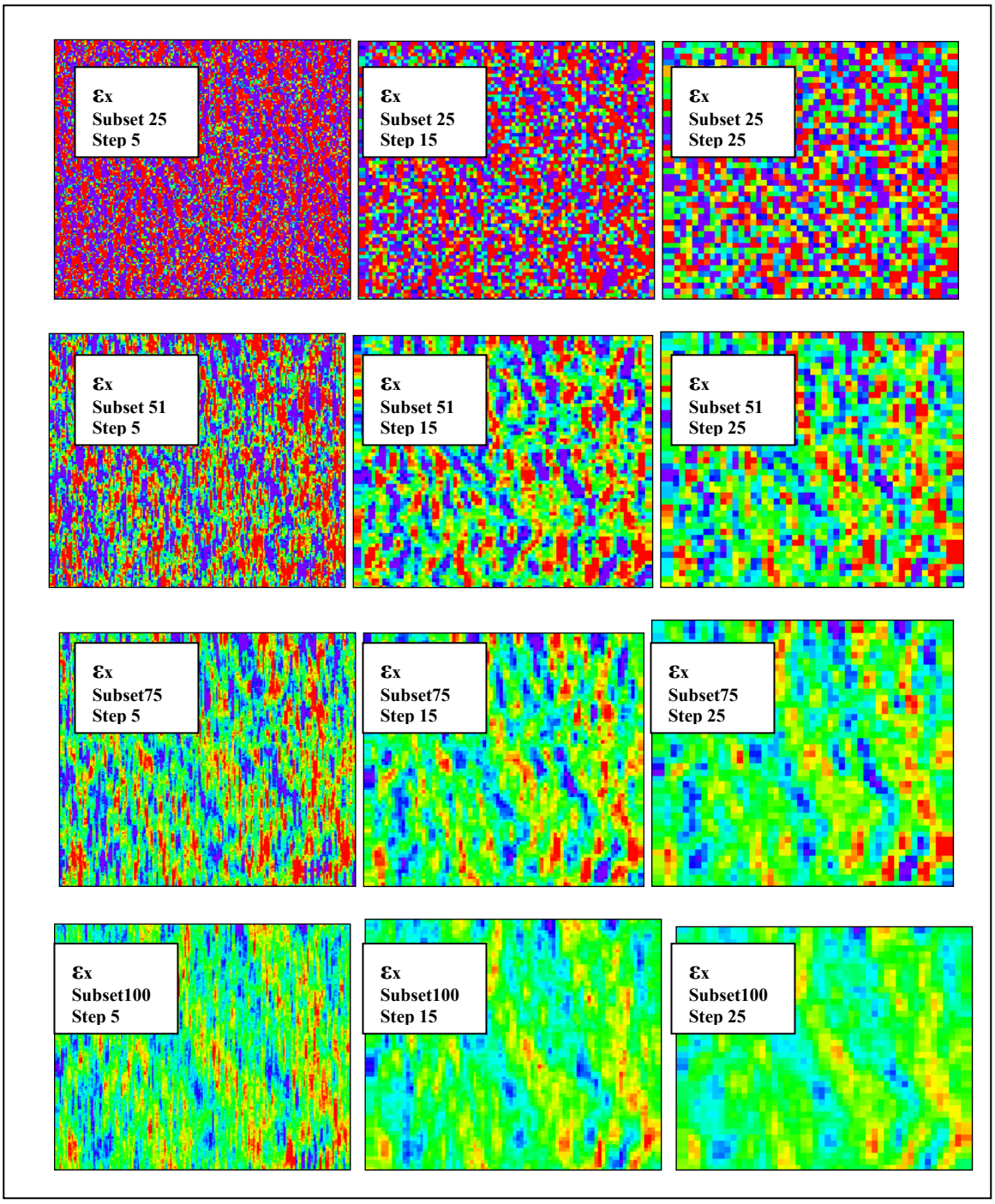

Figure 4.8 ε_x: Aluminum Bar DIC
Strain Range 6.0e2 to 1.2e3 με

Step Size Effects.

The step size effects seemed to be less significant than the subset size effects; however, the step size did have a direct effect on the grain structures noted within the strain fields produced using larger subset sizes. Variations were noted in the grain structure, which closely corresponded to the step size. These variations can be seen especially well in Figure 4.8 for the 75 pixel subset and the 100 pixel subset with step size of 5 pixels. The variations exhibit vertical striations of approximately the same width and spacing as the step size. Large shifts in strain over a very small distance are also noted. In both these figures it is not uncommon to see the strain range from the low end of the scale to the high end of the scale within only two or three steps; 10 to 15 pixels. With large step sizes; in this case 25 pixels, the grain structure began to take on a coarsely pixilated appearance, but the variations were softened. With intermediate step sizes the grain structures were less pixilated than the small step size but the variations were softened less than the large step size.

Composite Coupon

Transverse and shear strains were investigated for the composite coupon. General trends for the strains were taken from raster images of the entire AOI. The raster images were created by assigning colors to the varying values of strain in tables created during the data conditioning. Line graphs to investigate the strain about a vertical cut through the specimen were made. Moiré interferometry data for the line graphs were taken from a random cut through the thickness of the specimen. DIC data were chosen for the line graphs from the cut, which produced the closest match to the moiré data. Both moiré data and DIC data were compared against a solution by using the AFRL's B-SAM

technique. B-SAM is a 3-D strain analysis program. It is much like a Finite Elements (FE) program; however instead of the standard FE elements it uses B-spline approximation functions. It combines these B-spline functions into a three dimensional shape function. It has the advantages over standard FE methods of being very computationally efficient and boundary conditions can be enforced by specifying coefficients in the B-spline functions. (Schoeppner et al., 2004)

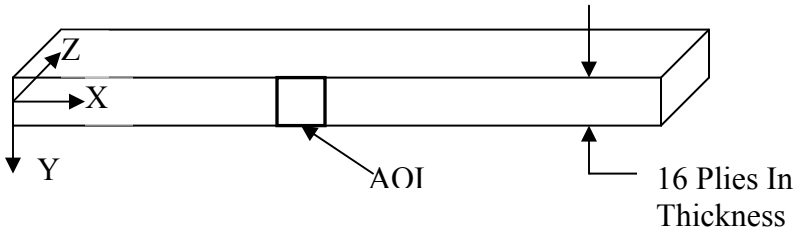

Figure 4.9 Composite Specimen

Subset Size Effects.

The effects of the subset size on the analysis of the composite coupon were found to be similar to those of the aluminum bar: the larger the subset the smoother the data became. The smoothing was apparent in both the displacement data and the strains (transverse and shear) derived from the displacements as displayed in Figures 4.10 through 4.17. Transverse and shear strains found with a subset measuring 25 pixels showed some of the stratification displayed by the moiré data, however they were also dominated by poor data quality. Transverse and shear strains calculated from the correlations with subsets measuring 50 and 75 pixels both displayed excellent stratification due to ply structure with little noise. Furthermore, the 50 and 75 pixel subsets resolved variation in the layers also shown in the moiré data. Transverse and shear strains developed from the correlation with subsets measuring 100 pixels displayed the stratification in the strains; however, some of the finer detail was lost. The large

subset size contributed too much smoothing action. Figures 4.18 and 4.19 show the moiré interferometry displacement fields and transverse and shear strains for comparison.

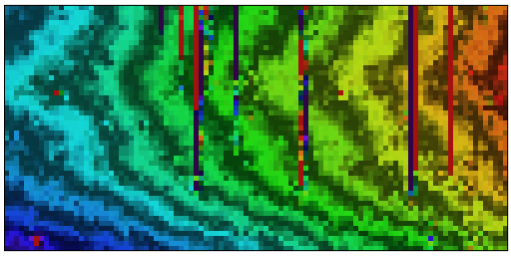

Figure 4.10a U Field: Composite Specimen DIC Subset 25 Step 10

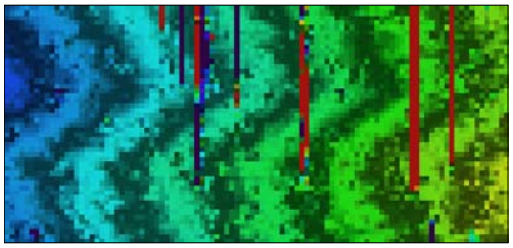

Figure 4.10b V Field: Composite Specimen DIC Subset 25 Step 10

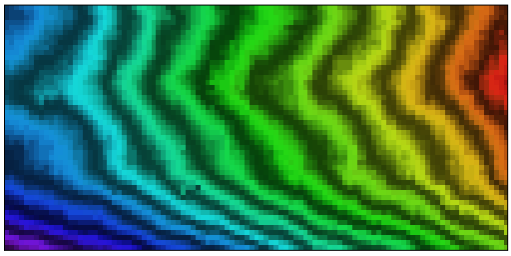

Figure 4.11a U Field: Composite Specimen DIC Subset 50 Step 10

Figure 4.11b V Field: Composite Specimen DIC Subset 50 Step 10

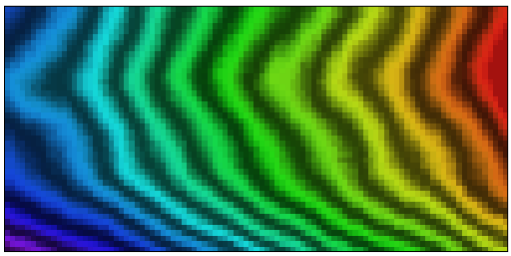

Figure 4.12a U Field: Composite Specimen DIC Subset 75 Step 10

Figure 4.12b V Field: Composite Specimen DIC Subset 75 Step 10

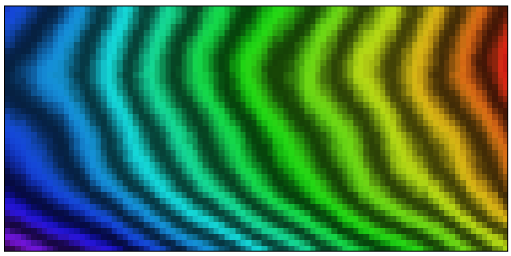

Figure 4.13a U Field Composite Specimen DIC Subset 100 Step 10

Figure 4.13b V Field: Composite Specimen DIC Subset 100 Step 10

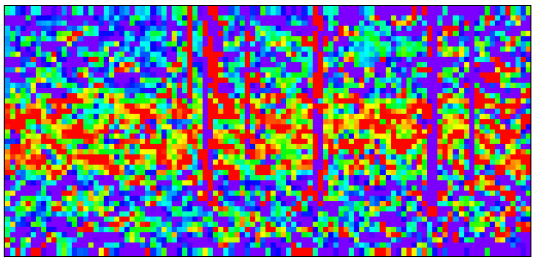

Figure 4.14a ε_y: Composite Specimen
DIC Subset 25 Step 10
Strain Range –2.799e3 to 4.637e3 με

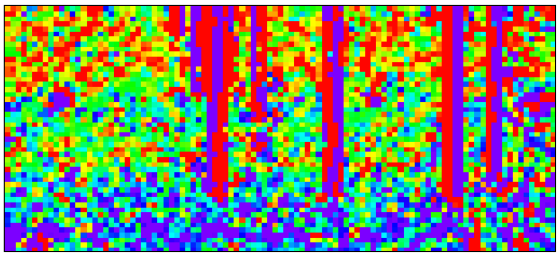

Figure 4.14b γ_{xy}: Composite Specimen
DIC Subset 25 Step 10
Strain Range -6.787e3 to 6.787e3 μγ

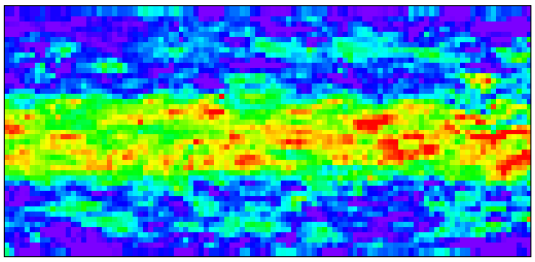

Figure 4.15a ε_y: Composite Specimen
DIC Subset 50 Step 10
Strain Range –2.799e3 to 4.637e3 με

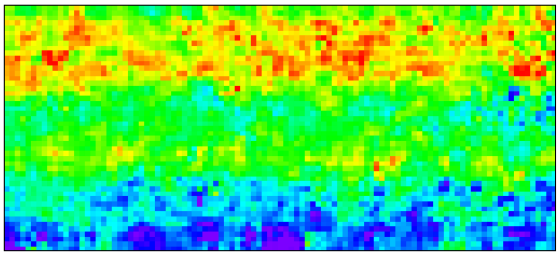

Figure 4.15b γ_{xy}: Composite Specimen
DIC Subset 25 Step 10
Strain Range -6.787e3 to 6.787e3 μγ

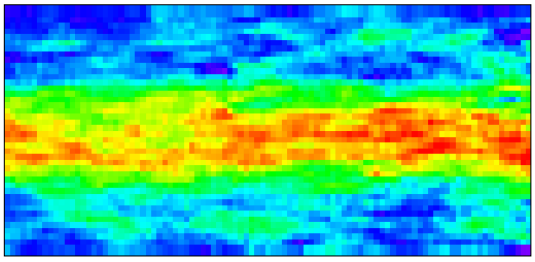

Figure 4.16a ε_y: Composite Specimen
DIC Subset 75 Step 10
Strain Range –2.799e3 to 4.637e3 με

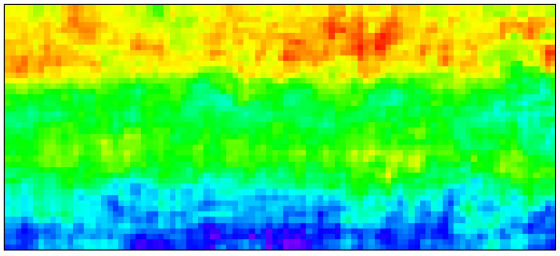

Figure 4.16b γ_{xy}: Composite Specimen
DIC Subset 75 Step 10
Strain Range -6.787e3 to 6.787e3 μγ

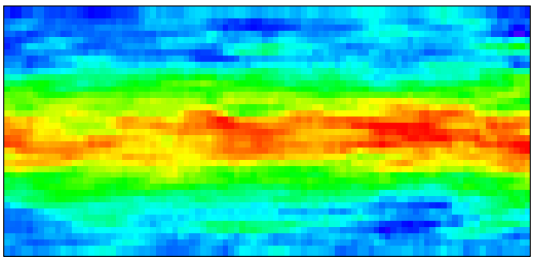

Figure 4.17a ε_y: Composite Specimen
DIC Subset 100 Step 10
Strain Range –2.799e3 to 4.637e3 με

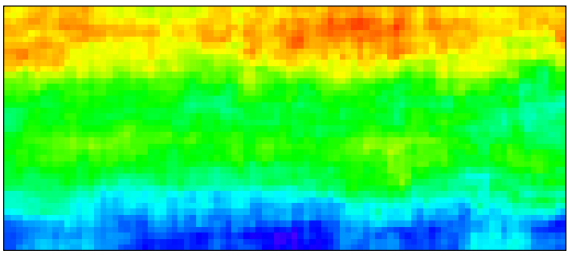

Figure 4.17b γ_{xy}: Composite Specimen
DIC Subset 100 Step 10
Strain Range -6.787e3 to 6.787e3 μγ

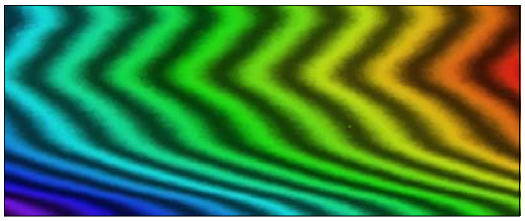

Figure 4.18a U Field: Composite Specimen Moiré Interferometry

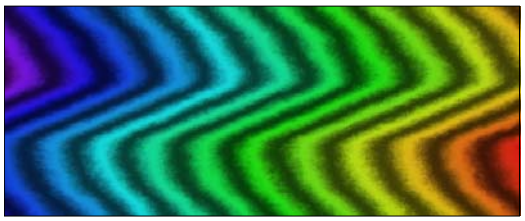

Figure 4.18b V Field: Composite Specimen Moiré Interferometry

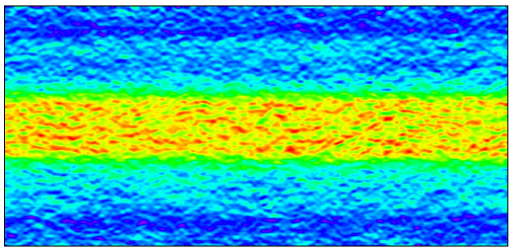

Figure 4.19a ε_y: Composite Specimen Moiré Interferometry

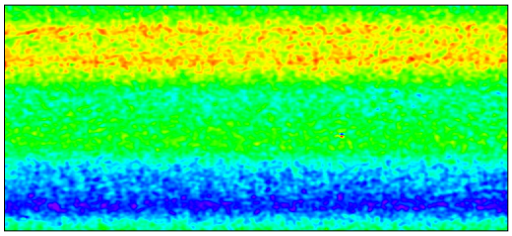

Figure 4.19b γ_{xy}: Composite Specimen Moiré Interferometry

To investigate the strains closer, line graphs made up of the strains for locations on a vertical line through the thickness of the specimen for each method were compared. The strain at any cut through the thickness should be identical since the fiber structure of the coupon was uniform along the length of the specimen. The line graphs for moiré interferometry and DIC were overlaid. The overlaid line graphs are shown in Figures 4.20 through 4.23 for the 50 and 75 pixel subset data. The results were very similar to those found from looking at the images in Figures 4.15, 4.16 and 4.19. The strains for subsets larger than 25 pixels showed trends closely matching the moiré data. Again, the 50 and 75 pixel sized subsets were the closest to the moiré data.

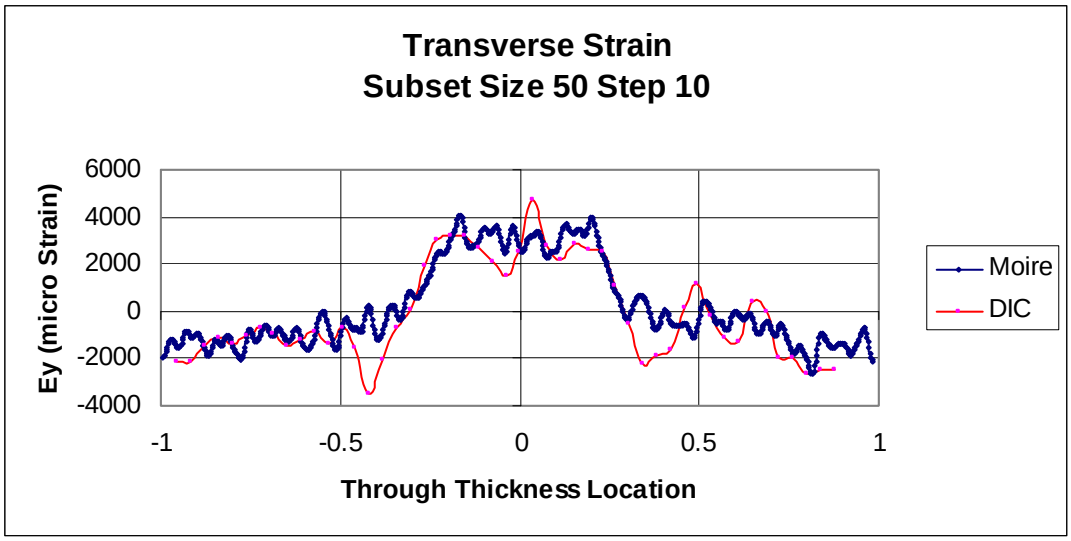

Figure 4.20 ε_y: Composite Specimen Moiré Interferometry and DIC Subset 50 Step 10

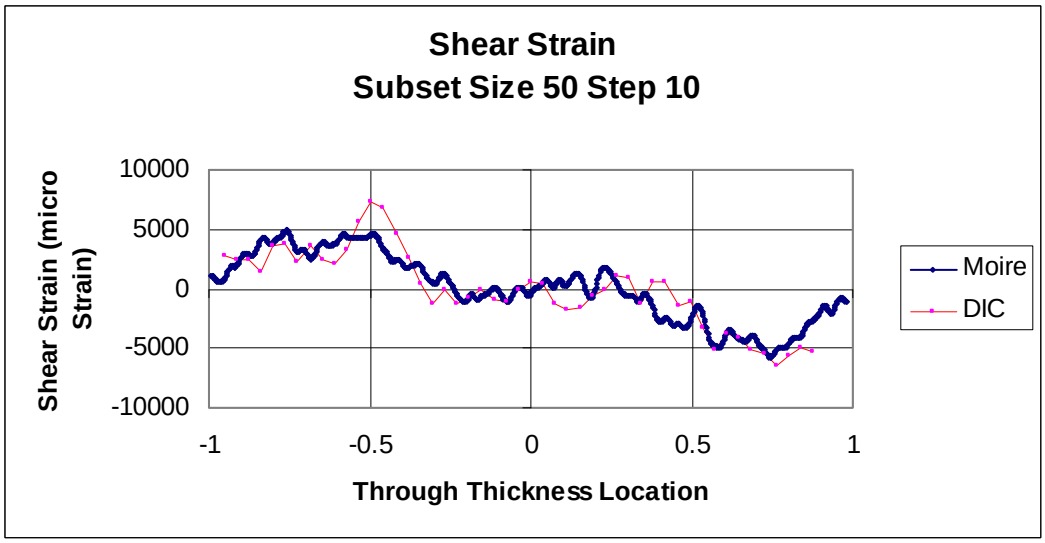

Figure 4.21 γ_{xy}: Composite Specimen Moiré Interferometry and DIC Subset 50 Step 10

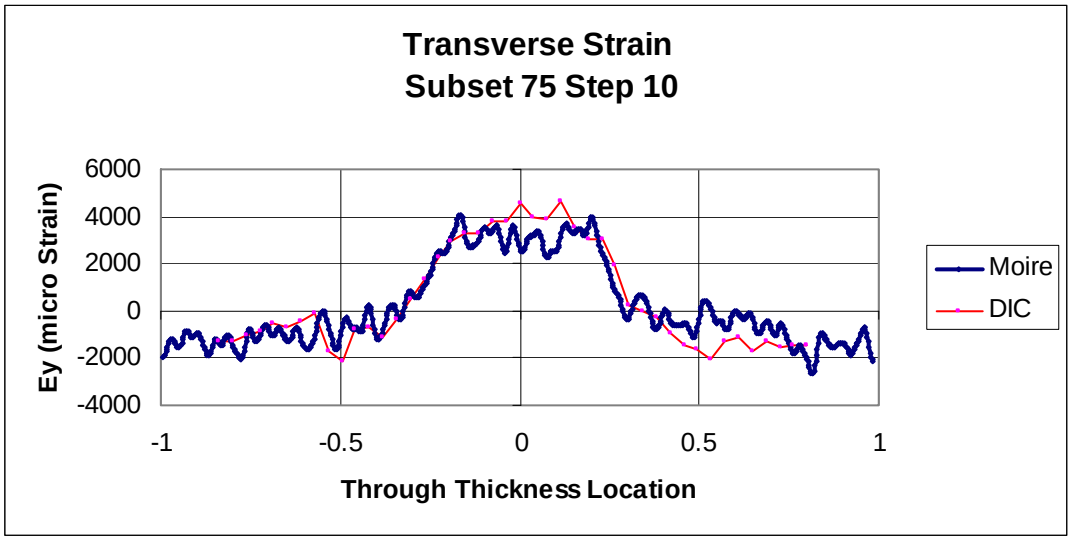

Figure 4.22 ε_y: Composite Specimen Moiré Interferometry and DIC Subset 75 Step 10

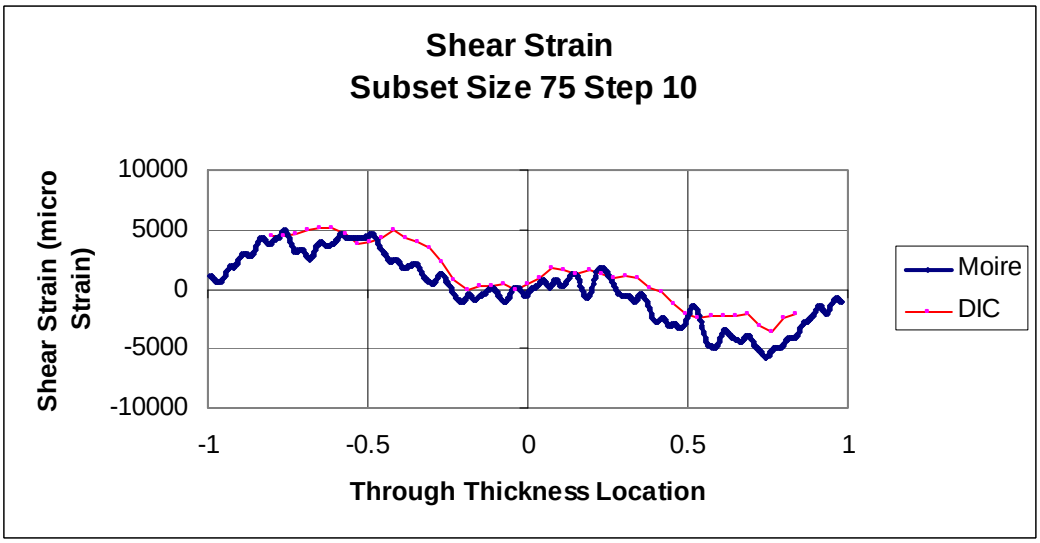

Figure 4.23 γ_{xy}: Composite Specimen Moiré Interferometry and DIC Subset 75 Step 10

Step Size Effects.

The step size had a more direct impact on the value of the strains measured for the composite coupon than they did for the aluminum bar. Again, with the 25 pixel step the data began to display obvious pixilation which removed peaks and filled valleys. The reduction in detail degraded the resolution to the point were peaks in the moiré data were not present in the DIC data. However, the general trend in the data remained very good. The line graphs of Figures 4.24 to 4.27 show the reduction in resolution between the 10 and 25 pixel step size for the 100 pixel sized subset data. Note that the peak transverse strain from the moiré data occurred at approximately 0.25 mm from the centerline, while for the DIC data with a 25 pixel step size the peak occurred at the centerline.

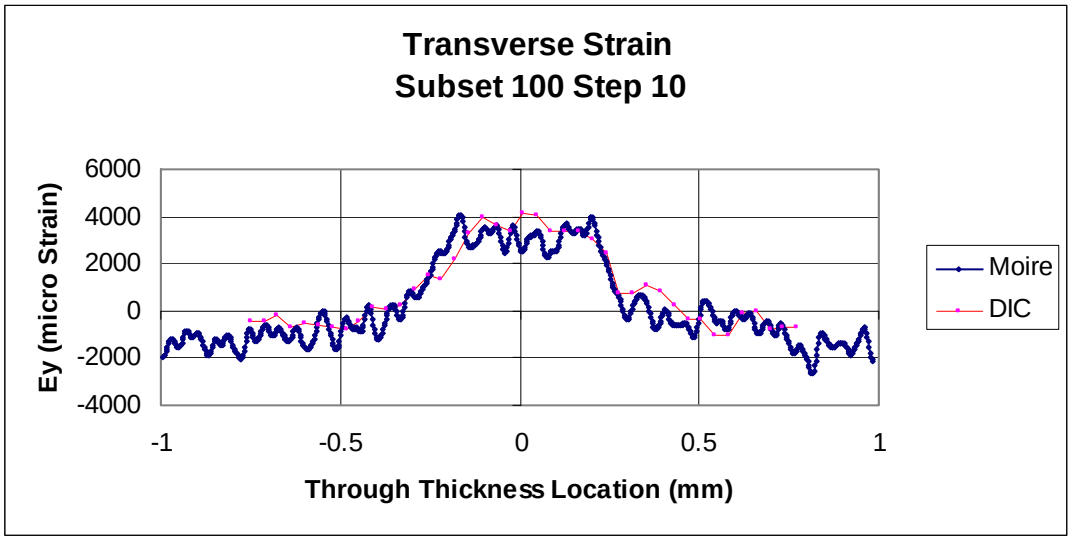

Figure 4.24 ε_y: Composite Specimen Moiré Interferometry and DIC Subset 100 Step10

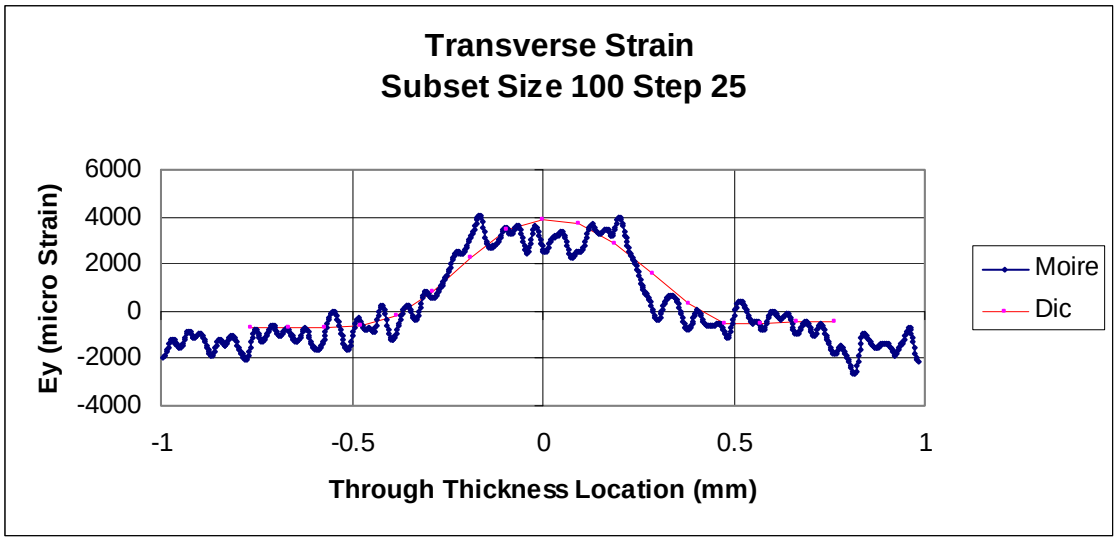

Figure 4.25 ε_y: Composite Specimen Moiré Interferometry and DIC Subset 100 Step 25

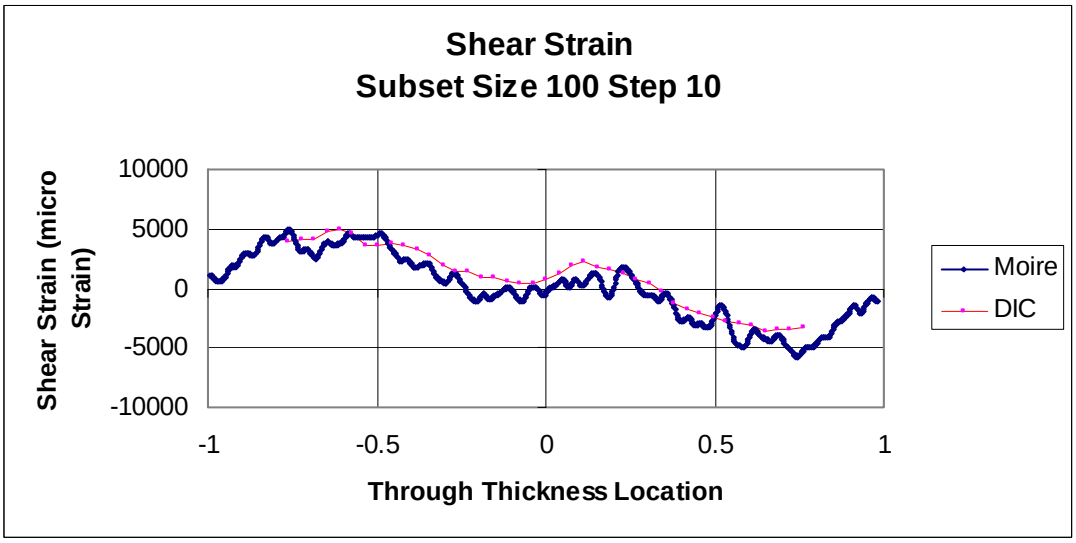

Figure 4.26 γ_{xy}: Composite Specimen Moiré Interferometry and DIC Subset 100 Step 10

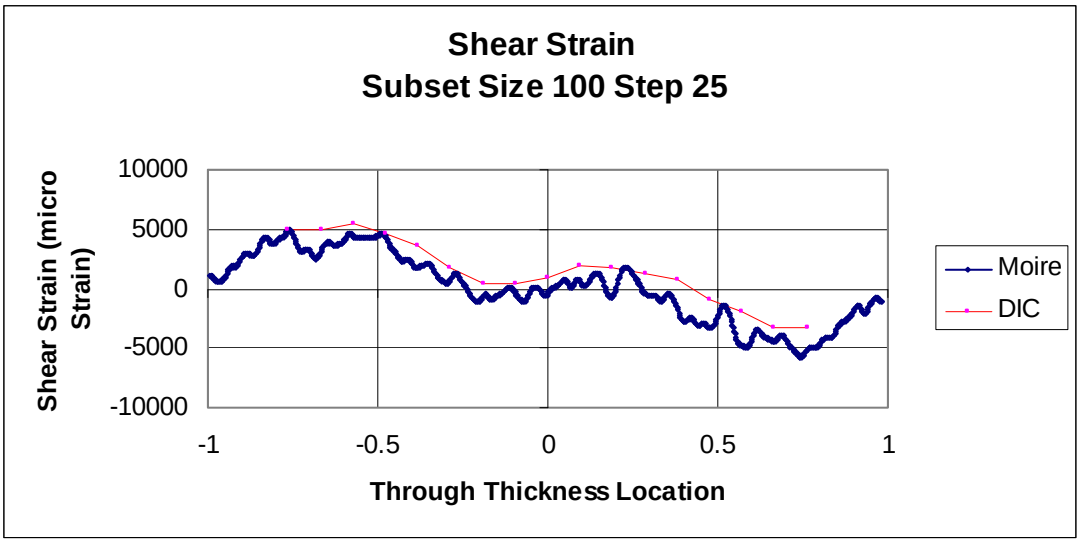

Figure 4.27 γ_{xy}: Composite Specimen Moiré Interferometry and DIC Subset 100 Step 25

B-SAM Solution.

Transverse and shear strains developed from the data collected in this study were compared to transverse and shear strains determined using the AFRL's B-SAM program. The strains from B-SAM were the product of a previous AFRL/RX study by Dr. David Mollenhauer. The general trends for transverse and shear strains for both moiré interferometry and DIC closely followed the results of the B-SAM study. This indicated that the grips did not slip as they did with the aluminum bar.

While the general trends matched nicely for all three methods, there were some differences in the data. B-SAM produced sharper corners in data, and more significant discontinuities between plies, as shown in Figures 4.28 through 4.31. The discontinuities can be explained by the fact that the B-SAM model contained perfectly straight fibers at the exact angles of the layup schedule, while the actual specimen contained the small variations in fiber straightness and direction expected in a composite panel laid up by hand. The strains from the DIC displacement data also showed some variations not seen

in the other data. Some of the more subtle trends in the B-SAM data were not present in the strains from the DIC data. These variations tended to change with subset and step sizes. As noted earlier larger subset and step sizes tended to smooth the data.

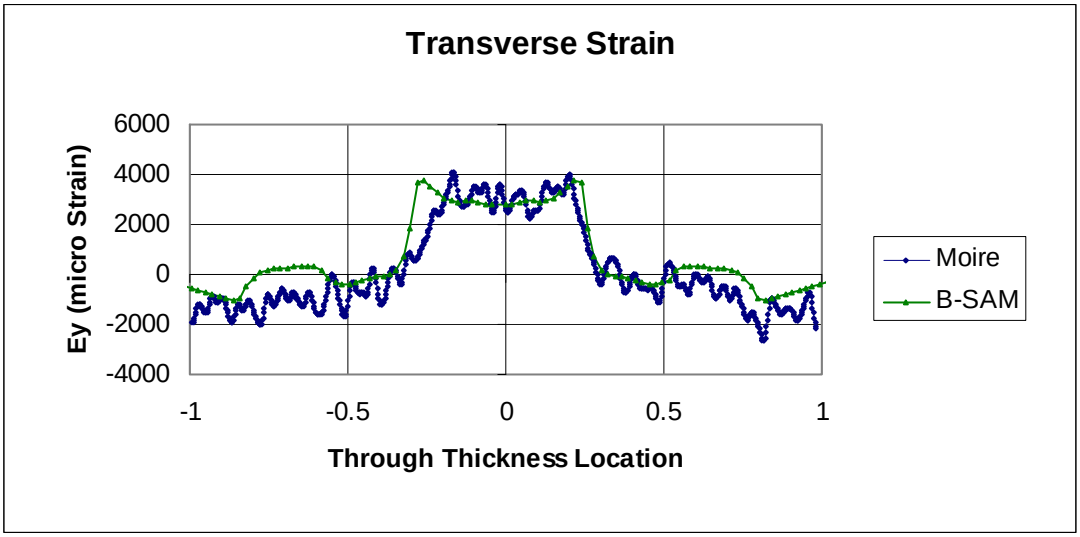

Figure 4.28 ε_y: Composite Specimen Moiré Interferometry and B-SAM

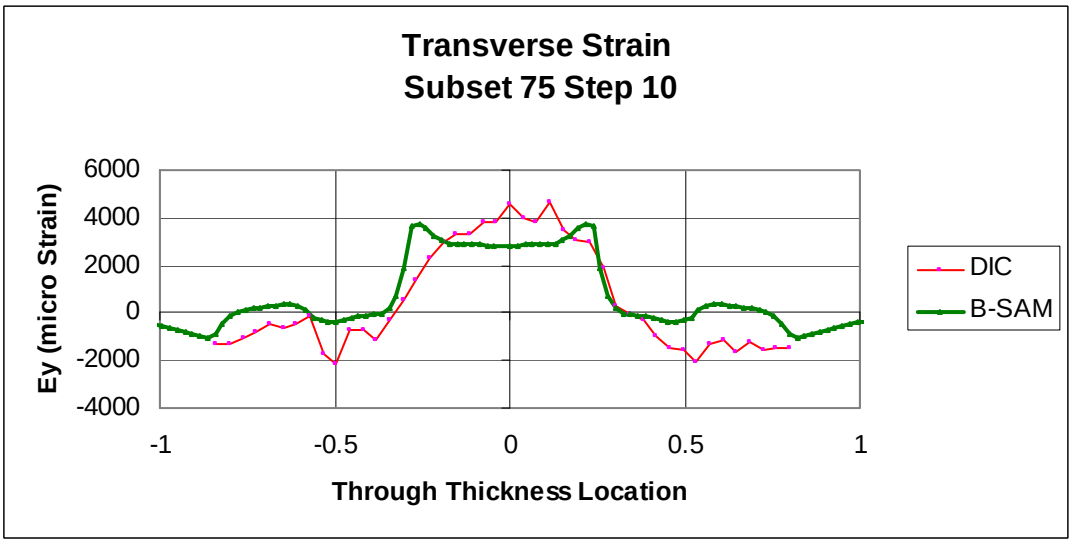

Figure 4.29 ε_y: Composite Specimen DIC Subset 75 Step 10 and B-SAM

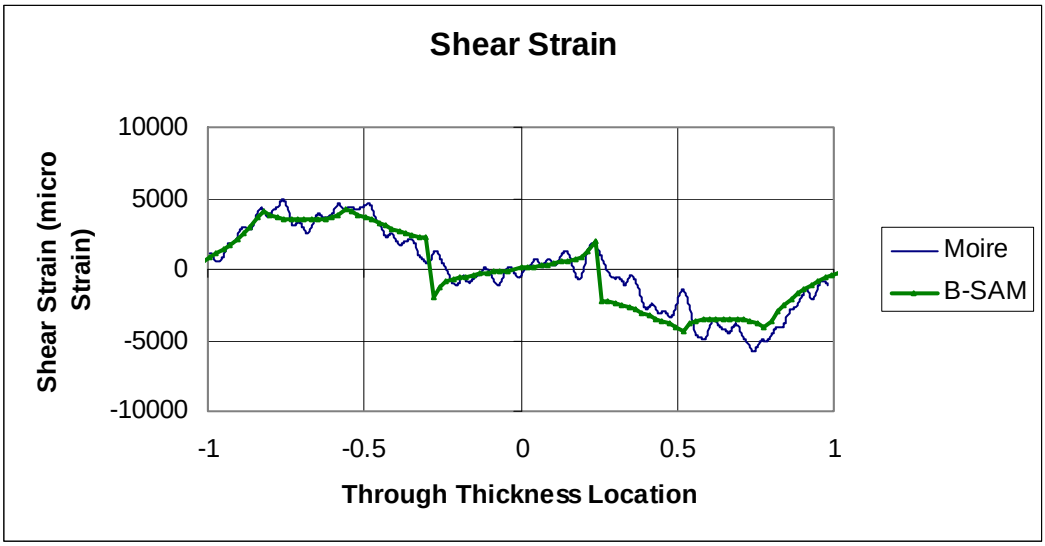

Figure 4.30 γ_{xy}: Composite Specimen Moiré Interferometry and B-SAM

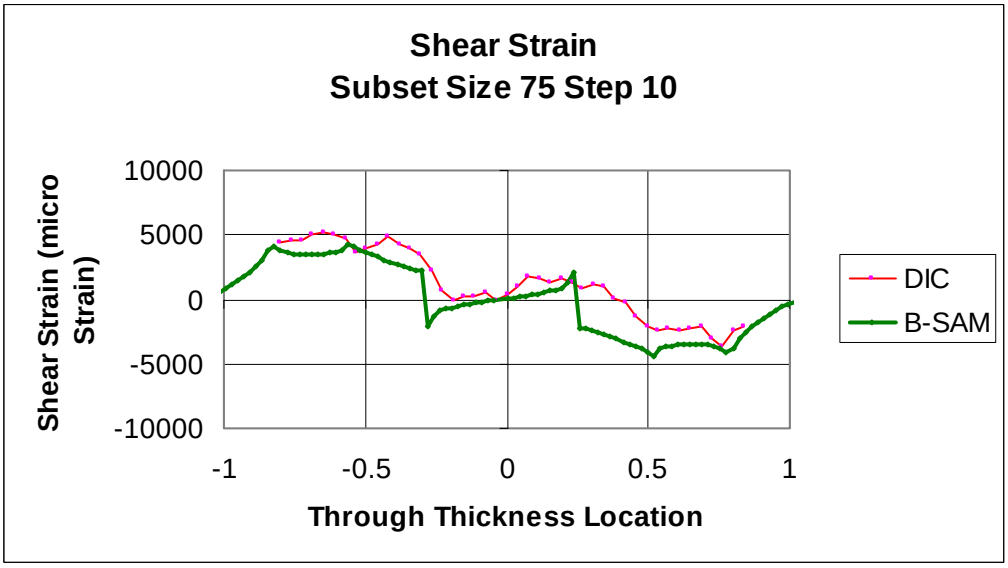

Figure 4.31 γ_{xy}: Composite Specimen DIC Subset 75 Step 10 and B-SAM

Strengths and Weaknesses of Each Method

Moiré interferometry and DIC have numerous strengths and weaknesses. Depending on the intended application, the impact of these properties will drive the researcher to or away from a particular method.

Moiré Interferometry Strengths.

First among moiré interferometry's strengths is its very high spatial resolution. As proven by Weissman and Post, moiré interferometry is capable of resolving displacements as small as 0.25 μm. Even at the limit of the spatial resolution, moiré produces fringes with excellent clarity and distinctness. While the resolution required for this study was not as fine as Weissman and Post showed, the method provided distinct strain fields for a very complex composite structure as shown in Figures 4.32 and 4.33.

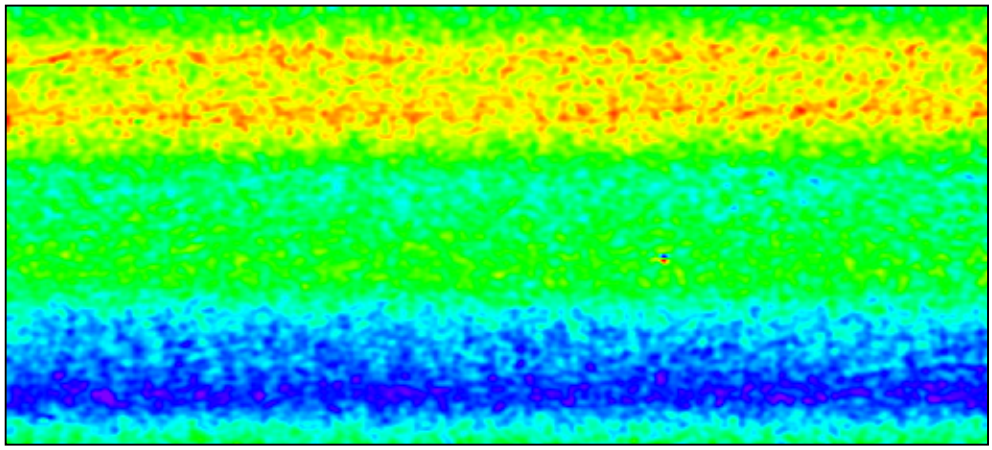

Figure 4.32 γ_{xy}: Composite Specimen Moiré Interferometry Strain Range -6.787e3 to 6.787e3 με

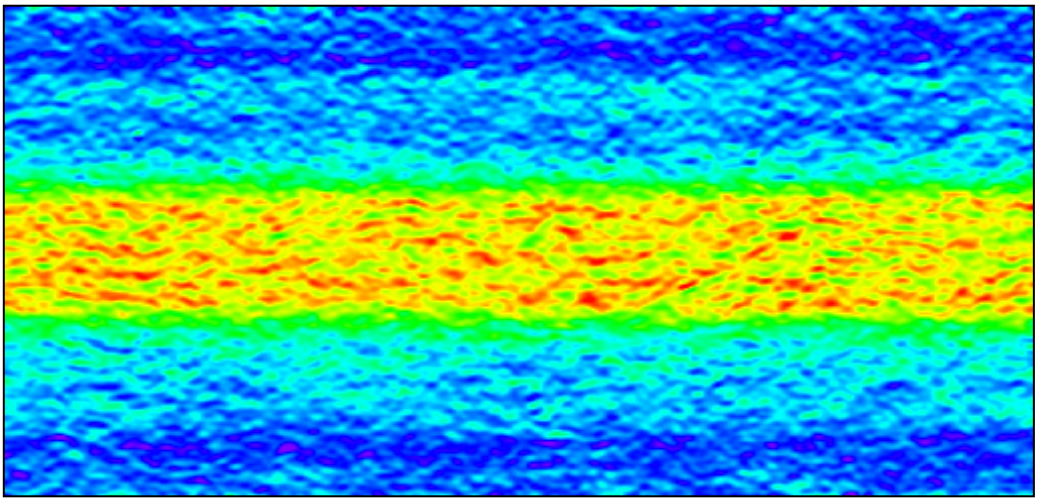

Figure 4.33 ε_y: Composite Specimen Moiré Interferometry
Strain Range –2.799e3 to 4.637e3 με

Second among moiré interferometry's strengths is the high level of insight into the workings of the method. The principles governing the basic method of moiré interferometry are simple enough to be understood by almost any engineer or scientist. The analysis of the data is straightforward as well, with strains easily found from the displacement fields. The high level of insight into moiré interferometry gives the researcher the capability to control almost every aspect of the process leading to high confidence in findings. What little automation is involved in moiré interferometry is not necessary, but a convenience.

Moiré Interferometry Weaknesses.

For its strengths, there are significant drawbacks to the method. First, while the very high sensitivity can produce results with incredible spatial resolution, the sensitivity also ties the method to the laboratory. The entire experimental setup must be isolated from all vibration. In this study, isolation was provided by the optical table to which the load frame, interferometer and camera were attached. Not only was the table exceedingly heavy and stiff, but the tabletop also rested on gas filled bladders which absorbed shocks

traveling from the building through the legs of the table. During the test, if the table was bumped the fringe pattern would be disturbed. In fact, the fringe pattern would be obliterated by as little as someone tapping the table with their fingers. Air currents caused by someone walking by the interferometer or someone opening a door across the room were also seen to affect the fringe pattern. The result of this sensitivity was that even in a very controlled environment data could only be taken if there was little or no activity in the laboratory except the moiré interferometry tests.

Figure 4.34 Vibration Isolated Optical Table Used for Moiré Interferometry Tests

The sensitivity of the method also leads to some very exacting requirements for grating quality and alignment. In all, four gratings were applied to the specimens. The first grating for the aluminum bar was unusable because of bubbles in the epoxy under the grating. This grating had to be sanded off the specimen and a new one applied. Two composite coupons were made, and a grating applied to each. One of these was also unacceptable because of an imperfect grating. All four gratings were applied with the supervision and assistance of an expert in the field and still only a 50% success rate was

achieved for grating application. Not only did the gratings have to be almost perfectly applied, they needed to be properly aligned. A somewhat complex alignment procedure was used to ensure the rows of each grating aligned with the axis of the specimen to which it was attached. The alignment fixture and process was described in Chapter 3. The alignment of the specimen to the interferometer had to be ensured once each specimen was attached to the load frame. A rotation of the specimen with respect to the interferometer would cause 40 fringes per mm for each degree of rotation.

As a consequence of user control over almost every portion of moiré interferometry, the method is very slow. No moiré interferometry test was performed for this study that took less than one day for set up and data collection. Data conditioning and analysis took significantly more time. Had the fringe pattern analysis been done by hand instead of with Superfringe, the data analysis would have taken weeks at best. The grating application was a very time intensive operation. The preparation of the specimen and application of the grating took several hours. After application of the grating, the epoxy was allowed 7 days to cure (to achieve full strength) before removal of the glass plate which contained the grating. If the grating was found to be unacceptable, then the application process would have to start over.

Digital Image Correlation Strengths.

Speed was the single most powerful advantage of DIC. Every step of DIC that was comparable to moiré interferometry required less time to perform. The speckle pattern applied to the aluminum bar was complete within 30 minutes. The 30 minutes included practice patterns applied to paper and cardboard. The first speckle pattern applied to the aluminum bar was acceptable. The composite coupon required at most two hours to

achieve an acceptable pattern. If the researcher is confident in the strain calculations performed by the image correlation program, results can be found within a very short period of time. After mounting the specimen in the load frame, it was possible to calculate strains within two hours. This two hours included capturing all calibration and load photographs, calibration of the system and calculation of strains. It should be noted that the strains used in this study were not calculated by VIC-3D 2006, and therefore took much more time than if they had been.

The three dimensional capability of DIC gives more insight into the mechanics of a problem than is provided by the strictly two dimensional moiré interferometry. The slippage of the grips, as discussed earlier are evidence of this. The out of plane displacement field produced by VIC-3D indicated that bending was occurring in the specimen. The bending was confirmed using a finite elements model. In addition to the insight provided to this study by out of plain displacements, the out of plain capability can be leveraged to study three-dimensional problems.

DIC is not tied to the laboratory and as such is very portable. The VIC-3D hardware included two cameras with associated optics, a light source and a laptop computer. As long as power can be delivered to the light source and laptop the experiment could be performed in almost any stable environment. A vibration isolation table is not required. In fact the composite coupon was tested on an optical table with no active vibration protection.

Digital Image Correlation Weaknesses.

The primary weakness of DIC is the lack of insight into the processes used within the image correlation software. As with all commercial software, some faith must be placed

in the methods used by the programmers if little or no documentation is provided with the software on the methods used. The lack of insight into the strain calculation process prompted the author to use only the displacement fields produced by VIC-3D, and not use the strains found by the program. This lack of insight extended the time required to find strains significantly. However, the confidence in the results of the study was much greater than it would have been possible using strain results from an unknown process.

Numerous other small weaknesses should be noted because of their effect on results, or on their effect on the test preparation. The displacement data produced by DIC tended to be very prone to noise and data scatter. While the noise tended to reduce with increased subset size and step size, the expense of this was reduced sensitivity to small changes in the strain fields. The speckle pattern for high magnification tests was very difficult to apply. The author suspects that an optimal pattern was never achieved. Not only are very small speckles difficult to produce for high magnification tests, but as the magnification increases the height of the speckle becomes apparent. For speckles produced with paint, each speckle was shaped like half a sphere, with the height of each speckle clearly visible under a binocular microscope. Last, the DIC system is very sensitive to changes to camera location and orientation after the calibration photographs have been captured. The system is so sensitive in fact, that if the camera cords are bumped, an accurate correlation may not be possible. Correlated Solutions attempted to remedy this situation with a secondary calibration based on speckle photos. The secondary calibration was used to improve the calibration of the system, but never because the cameras were bumped or repositioned.

V. Conclusions and Recommendations

Summary

This study was intended to compare DIC and moiré interferometry, and to also determine the effects of subset size and step size. Strains developed from DIC measured displacement fields compared favorably with strains developed from moiré interferometry measured displacement fields. The effects of the subset size and step size were qualitatively determined for both an isotropic specimen and a composite coupon with a complex ply arrangement.

Accuracy of DIC.

Strain fields were determined for two specimens using both DIC and moiré interferometry. The displacement data from moiré interferometry were resampled to match the resolution of DIC measurements for the same specimen. Strains were then calculated from both sets of displacement data and the means of the strain fields were compared. Approximately ten percent difference of the mean axial strains separated the two methods. However, there was an error of unknown magnitude in both the moiré interferometry and DIC displacement data caused by the grip slipping on the specimen. The error was suspected to be greater in the moiré interferometry displacements than the DIC displacements. The trends of the transverse and shear strains for the composite coupon for both moiré interferometry and DIC were very close to one another. Additionally, the AFRL's B-SAM program produced transverse and shear strains, which confirmed the accuracy of both data sets. Grip slippage could be prevented in future tests by applying a load to the specimen, which cycled between almost zero load and the load

frame maximum load. After a number of load cycles; probably less than ten, the specimen would be set in the grips.

Subset Size and Step Size Effects.

Numerous displacement data sets were created by varying both subset and step sizes when the DIC correlations were run. Effects of subset and step sizes were clearly seen in the displacement and strain fields. Larger subset sizes tended to reduce noise by smoothing the data for both displacement and strain fields. For the composite coupon, both a 50 pixel and 75 pixel subset size produced excellent strain fields. Subset sizes larger than this tended to cause the data to be smoothed to the point of loosing detail. The effect of the step size was to reduce detail in the data by coarsening the pixilation of the displacement and strain fields. Unlike the subset size, instead of improving the results by increasing the size, the larger step sizes tended to remove peaks and valleys in the data. With the larger step sizes, some peak strains were found to occur in erroneous locations because of the reduction in detail.

Effect of Speckle Size on Subset Size.

The size of the speckles; as seen in the photographs differed drastically between the two specimens. The typical speckle on the composite coupon was much larger when measured in pixels than that of the typical speckle of the aluminum bar. There was also less variation in the size of speckle on the composite coupon. The minimum effective subset size for the aluminum bar was 25 pixels, while the minimum effective subset size for the composite coupon was 50 pixels. The author suspected that the speckle size influenced the smallest subset, which would provide uncorrupted data. While a sufficient

number of speckle patterns were not tested to define a standard for a subset size to speckle size ratio, the data did indicate that the ratio would be at least two.

Subset Size and Step Size Combinations.

Many subset size and step sizes combinations were used when producing the DIC displacement data. It was found that if the step size was larger than the subset size, the correlation would have many areas with data missing. The data dropout was suspected to occur in areas where the subsets did not overlap because of the large step. It is suggested that researchers always use step sizes smaller than the subset.

The main advantage of DIC over moiré interferometry is the method's speed. The entire process, from specimen preparation to data analysis is far faster than the process for moiré interferometry. If the researcher is comfortable with the strain analysis of the DIC program, the time savings are even greater. If results are needed quickly, then the researcher should use DIC.

The portability of DIC could also be a major advantage to a researcher. A DIC test should be able to be performed in almost any location, as long as a power can be provided to the system and there is a surface stable enough to support the cameras. The system is; however, very sensitive to camera movement after calibration photos have been taken. The researcher conducting a DIC test outside a building may want to secure the camera wires to the camera supports to prevent movement in windy conditions. The portability and lack of sensitivity to the environment may allow the analysis of structures in their intended surroundings.

Cost.

The initial investment to procure the components for both moiré interferometry and DIC were remarkably similar; approximately $100,000. However, the expense of the supplies to conduct tests differ greatly. Each diffraction grating used in this test cost approximately $100. In total, three gratings were used for an expense of $300. Less than ten dollars worth of paint would be enough for a very large number of speckle patterns. (Mollenhauer,2008)

Strengths of Moiré Interferometry.

Throughout this test, moiré interferometry proved to have at least a slightly higher spatial resolution than DIC. Additionally, moiré interferometry had much less scatter in the displacements measured and in the strains produced from them. If very high fidelity data is the overriding requirement for data produced in the test, then moiré interferometry should be used.

Additional strengths of moiré interferometry are the visibility into the processes and the researcher's control over almost every aspect of the test. The theory behind the method is straightforward, and equations used in the calculation of displacement fields and strains are very simple. The insight into moiré interferometry and the amount of control that the researcher has should lead to high confidence in results produced from the method.

Conclusions

Listed below are the conclusions drawn from the execution of this study. Additionally, Table 5.1 is a very condensed version of many of the results of this study.

It has been provided to assist future researchers decide between moiré interferometry and digital image correlation.

Conclusion 1.

DIC provides results to within approximately ten percent of both moiré interferometry and the theoretical solution for a simple strain field. For more complex strain fields, DIC agrees very closely with other accepted methods of strain field analysis.

Conclusion 2.

Small subset sizes produce data dominated by noise. Intermediate to large subsets sizes tended to reduce noise while maintaining detail by smoothing data. Very large subsets are capable of smoothing the data to the point where detail is lost.

Conclusion 3.

Small step sizes produced strains, which closely matched results derived from other methods. Larger step sizes tended to reduce the detail present in the data, even to the point of changing the trend of the data and causing erroneous maximum strain locations.

Conclusion 4.

The size of the speckles in the DIC photographs influenced the size of the smallest subset, which would produce useable data. The larger the speckle, the larger the subset needed to be to produce valid data.

Conclusion 5.

Subset size and step size combinations where the step was larger than the subset caused areas to occur which had no data, or erroneous data associated with them. The researcher should always use subsets that are larger than the step.

Conclusion 6.

DIC has the capability to provide results very quickly. If the researcher has an overriding need to develop results quickly, then DIC should be used.

Conclusion 7.

DIC is a highly portable system, which is not limited to use in the laboratory. If a test is required to be performed outside, or in an environment not isolated from vibration, wind currents or excessive light, then DIC should be used.

Conclusion 8.

Both moiré interferometry and DIC require an initial investment of approximately $100,000 to buy the respective system, however the cost associated with each test is much less for DIC.

Conclusion 9.

The spatial resolution of DIC did not appear to be as high as moiré interferometry. If a very high spatial resolution is required, then moiré interferometry should be used.

Table 5.1 Method Selection Quick Reference

If This Condition Is Required	Then Use This Method	Remarks
Low Scatter in Data	Moiré Interferometry	Moiré Interferometry produces displacement data more tightly grouped around the mean.
High Spatial Resolution	Moiré Interferometry	Moiré Interferometry has at least slightly higher spatial resolution
Results Quickly	Digital Image Correlation	Every step of DIC is quicker than similar steps in moiré interferometry. If the strain calculations if the DIC program are trusted, strains can be determined within hours of the start of a test.
Non Laboratory Environment	Digital Image Correlation	DIC is not tied to the laboratory as is the case with moiré interferometry. DIC can be used in almost any location where power is available and a suitable surface is present for camera support.
Three Dimensional Results	Digital Image Correlation	DIC is capable of 3-D analysis where moiré interferometry is not.

Recommendations

Although this study attempted to determine the spatial resolution of DIC, much room remains for further testing. Listed below are two suggestions for future testing of DIC. The first fills the gap between the simple strain field and the complex strain field tested for this study. The second may be able to quantify the effects of subset size and step size on spatial resolution.

Test an Intermediately Complex Strain Field.

An intermediately complex strain field was planned to have been tested for this study. The specimen would have been an aluminum bar, much like the one tested however, with a 0.635 cm hole drilled through the center of the face of the specimen. Equipment failure and time constraints prevented this specimen from being tested. The results provided by this specimen may provide more insight into the effect of the subset size and step size.

Quantify Spatial Resolution and the Effect of Subset Size and Step Size.

Towards the end of the analysis, the author and David Mollenhauer determined a method to quantify the spatial resolution of DIC. This method was not included in the test presented here and is left for future research. The specimen for future testing shown in Figure 5.1 would be a bar made of an isotropic material, much like the aluminum bar tested for this study. The bar would have many holes drilled along the center of the face of the specimen. The holes on one half of the bar would be the same diameter; however the space between the holes would decrease. This would produce a strain field with irregularly spaced peaks. The holes in the other half of the bar would consist of pairs of holes with decreasing diameter between each set. The holes in all pairs would have the same spacing, for example, 2.25 diameters. The spacing would be set such that the peaks of the strain field induced by the holes would have smaller and smaller spacing. The limit of spatial resolution of the method would be achieved when the method could no longer resolve the two strain peaks. The effect of subset size and step size on spatial resolution could be directly determined.

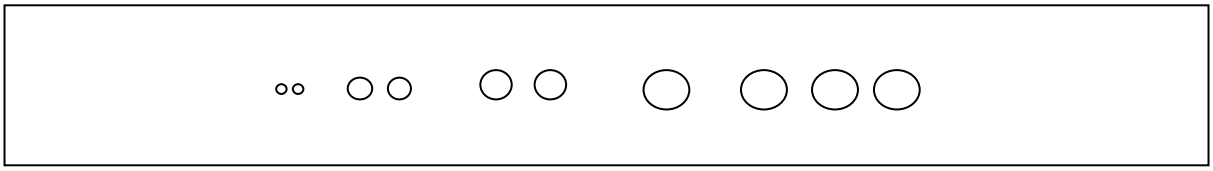

Figure 5.1 Proposed Specimen to Find Spatial Resolution

Appendix A

Lessons Learned

Over the course of the study, a few lessons were learned about DIC that would speed the progress of a researcher new to the method. While not necessarily unknown to the community as a whole, the following tips were not found in the literature.

Speckle Pattern and Magnification.

Speckle patterns were easy to apply to specimens that were not used for high magnification tests. As the magnification increased, the application a high quality speckle pattern became much more difficult. At low levels of magnification spray paint procured at any hardware store was acceptable. The plume of paint was easily directed such that speckles covered about 50% of the surface and that the size and shape of each speckle was random. When higher levels of magnification were used, the spray paint produced only a marginally acceptable pattern. If the speckle pattern was applied in the same manner as for lower magnification tests the pattern would turn out to be almost entirely covered by very few large speckles. The paint plume should be directed past the specimen for minutes with almost no paint settling on the specimen. This was how the speckle pattern was applied to the composite coupon in this study. This method produced many speckles that were large relative to the very few other speckles on the specimen. This method also wasted an inordinate amount of paint. The reason for the apparent larger speckles on higher magnification tests was that although the individual speckles were probably of about the same size as those applied to the low magnification specimen, a single speckle occupied many more pixels on the high magnification photographs than the same speckle would have on the low magnification photographs.

A potentially better method of applying a speckle pattern to a high magnification specimen would be to thin a small amount of paint; using paint thinner or acetone, and use an airbrush to apply the speckle. The paint jet would still not be pointed directly at the specimen, but would be directed across the specimen with droplets falling onto the specimen. The speckle pattern applied to the composite specimen shown in Figure A.1 was produced in this manner. Note also that the speckles are white and that the background is the natural color of a graphite/epoxy composite. This speckle pattern was not tested because of time constraints.

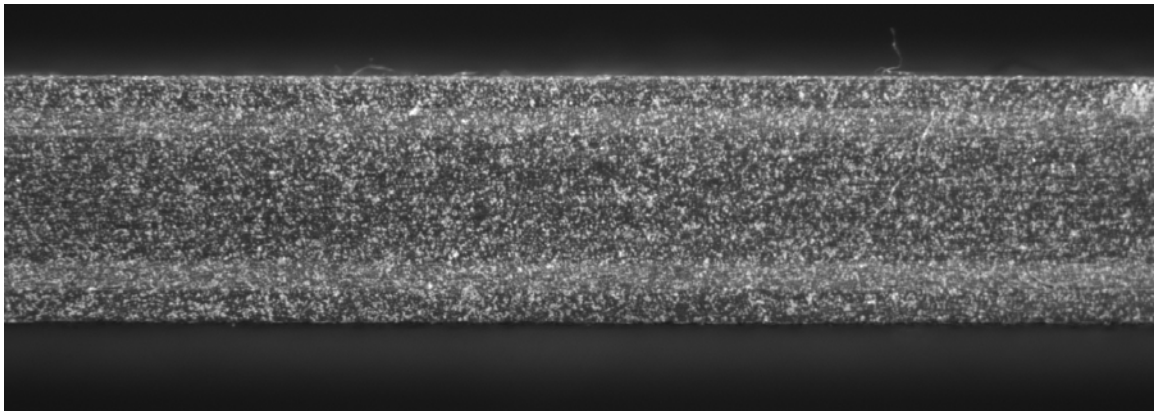

Figure A.1 Results of Alternate Speckle Application Method

Calibration Target Photographs.

A good calibration of the DIC system was crucial to accurate image correlations. To achieve a proper calibration the target should be photographed at numerous locations and at numerous rotations. Photographs should be taken with the target rotated such that the left or right edge is closer to the camera and the rotation is large enough to be noticeable in the pictures. The rotation appears in the picture as a skew of the grid to one side or the other such that the square grid appears to be a rhombus. The target should be translated

perpendicular to the camera between successive photographs. Without rotations the program will not have enough data to solve the system of calibration equations.

If the target used for calibration is constructed of glass with all but the dots covered by a mirror surface; such as the targets used for this test, a light should be projected through the target such that the dots are illuminated from behind. Additionally, the light and shutter speed should be set so the image is saturated at the dot locations. This saturation serves two purposes. First, dots will appear to stay in focus at further displacements from the point of focus. This allows greater rotations of the target, especially when using very high magnification. Second, Vic-3D 2006 seemed to extract the locations of the points with less user input when the dots were saturated on the photograph. The suggestion to saturate the photographs was given by technical support at Correlated Solutions.

Mounting the calibration target to an X-Y traverse made the collection of calibration photographs quicker and more convenient. The target could be set to an angle, a photograph captured and the target translated by a small amount for another photograph. A very large number of pictures can be taken in a small amount of time using this arrangement. Additionally, since the target is mounted to a rigid structure there will be no movement of the target to blur the photographs.

Subset Size/Speckle Size Relationship.

The smallest useful subset size for the aluminum bar and the composite coupon were drastically different. The aluminum bar produced acceptable data when a subset of only 25 pixels was used. The composite coupon required a subset of approximately 50 pixels to give meaningful data. The disparity between the two effective subset sizes may be

caused by the speckle pattern. A measurement of a few representative speckles from the composite specimen revealed that the speckles were approximately 25 pixels in diameter. This would indicate the subset needs to be approximately twice as large as the average speckle.

Larger steps than subsets can cause data dropout.

Correlations were run that were not included in the analysis because of excessive data dropout. The commonality between these correlations was that the step size was larger than the subset size. After looking at the data briefly, it was realized that the data dropout should have been expected. A step size slightly larger than the subset size causes areas with only one subset covering them. If the step size is much larger than the subset size there will be areas of the AOI that are not covered by a subset. These areas not covered by a subset will have no displacement data associated with them.

Bibliography

Bing, Pan, Xie Hui-min, and Dai Fu-long. "Performance of Sub-Pixel Registration Algorithms in Digital Image Correlation," *Measurement Science and Technology*, 17: 1615-1621 (2006).

Bruck, H. A., S. R. McNeill, M. A. Sutton and W. H. Peters. "Digital Image Correlation Using Newton-Raphson Method of Partial Differential Correction," *Experimental Mechanics*, 29(3): 261-267, (September 1989).

Chu, T. C., W. F. Ranson, M. A. Sutton and W. H. Peters. "Applications of Digital-Image-Correlation Techniques to Experimental Mechanics," *Experimental Mechanics*, 25(3): 232-244, (September 1985).

De Nicola S., P. Ferraro, A. Finizio, G. Pierattini. "Fourier Transform Method of Fringe Analysis For Moiré Interferometry," *Proceedings of SPIE*, 4016: 35-40 (December 1999).

Han, Bongtae, Daniel Post and Peter Ifju. "Moire Interferometry For Engineering Mechnics: Current Practices and Future Developments," *Journal of Strain Analysis For Engineering Design*, 36(1): 101-117 (2001).

Helm, Jeffrey D., M. A. Sutton and S. R. McNeill. "Three-Dimensional Image Correlation for Surface Displacement Measurement," *SPIE Viedeometrics III, Proceedings of SPIE* (2350): 32-45, (October1994).

Helm, Jeffrey D., S. R. McNiell and M. A. Sutton. "Improved Three-dimensional Image Correlation for Surface Displacement Measurement," *Optical Engineering*, 35(7): 1911-1920, (July 1996).

Iarve, Endel. Research Engineer, University of Dayton Research Institute, Dayton OH. Personal Interview. (30 January – 4 February 2008).

Kahn-Jetter, Z. L. and T. C. Chu. "Three-Dimensional Displacement Measurements Using Digital Image Correlation and Photogrammic Analysis," *Experimental Mechanics*, 30(1): 10-16 (March 1990).

Lassahn, Gordon D., J. K. Lassahn, P. L. Taylor and V. A. Deason. "Multiphase Fringe Analysis with Unknown Phase Shifts," *Optical Engineering*, 33(6): 2039-2044, (June 1994).

Luo, P. F., Y. J. Chao, M. A. Sutton, and W. H. Peters. "Accurate Measurement of Three-dimensional deformations in Deformable and Rigid Bodies Using Computer Vision," *Experimental Mechanics*, 33(2): 123-132 (June 1993).

Mollenhauer, David H. and John Tyson. "Comparison of Moire Interferometry and Image Correlation Deformation Measurement Techniques," *Society of Experimental Mechanics Proceedings*, (2004).

Mollenahuer, David H., B. M. Fredrickson, G. A. Schoeppner, E. V. Iarve and A. N. Palazotto. "Moiré Interferometry Measurements of Composite Laminate Repair Behavior: Influence of Grating Thickness on Interlaminar Response," *Composites Part A: Applied Science and Manufacturing*, (In Press).

Mollehnhauer, David H. Research Engineer, Air Force Research Laboratory, Wright Patterson AFB, OH. Personal Interview. (14 February 2008).

Oster, Gerald and Yasunori Nishijima. "Moiré Patterns," *Scientific American*, 208(5): 54-63 (1963).

Post, Daniel. "Developments in Moire Interferometry," *Optical Engineering*, 21(3): 458-467 (May/June 1982).

Post, Daniel. "Moire Interferometry For Deformation and Strain Studies," *Optical Engineering*, 24(4): 663-667 (July/August 1985).

Post, Daniel; Bongtae Han and Peter Ifju. *High Sensitivity Moiré: Experimental Analysis for Mechanics and Materials*. New York: Springer-Verlag Inc., (1994).

Rayleigh. "On the Manufacture and Theory of Diffraction-Gratings," *London, Edinburgh, and Dublin Philosophical Magazine*, Series 4, 47(310): 81-93, (February 1874).

Schoeppner, G. A., D. H. Mollenhauer and E. V. Iarve. "Prediction and Measurement of Residual Strains For a Composite Bonded Joint," *Mechanics of Composite Materials*, 40(2): 119-133 (February 2004).

Sutton, M. A., W. J. Wolters, W. H. Peters, W. F. Ranson, and S. R. McNeill. "Determination of Displacements Using An Improved Digital Image Correlation Method," *Image and Vision Computing*, 1(3):133-139 (August 1983).

Walker, Colin A. "A Historical Review of Moiré Interferometry," *Experimental Mechanics*, 34(4), 281-299 (December 1994).

Weissman, Eric M. and Daniel Post. "Moire interferometry near the theoretical limit," *Applied Optics*, 21(9): 1621-1623 (May 1982).

Weisstein, Eric W. "B-Spline," *Mathworld*, http://mathworld.wolfram.com/B-Spline.html (4 February 2008).

REPORT DOCUMENTATION PAGE

Form Approved
OMB No. 0704–0188

1. REPORT DATE (DD–MM–YYYY)	2. REPORT TYPE	3. DATES COVERED *(From — To)*
27-03-2008	Master's Thesis	Mar 2007 — Mar 2008

4. TITLE AND SUBTITLE

A Comparison Of Moiré Interferometry And Digital Image Correlation

5a. CONTRACT NUMBER

5b. GRANT NUMBER

5c. PROGRAM ELEMENT NUMBER

6. AUTHOR(S)

Davidson, Ryan, J., Capt, USAF

5d. PROJECT NUMBER

5e. TASK NUMBER

5f. WORK UNIT NUMBER

7. PERFORMING ORGANIZATION NAME(S) AND ADDRESS(ES)

Air Force Institute of Technology
Graduate School of Engineering and Management (AFIT/EN)
2950 Hobson Way
WPAFB OH 45433-7765

8. PERFORMING ORGANIZATION REPORT NUMBER

AFIT/GAE/ENY/08-M06

9. SPONSORING / MONITORING AGENCY NAME(S) AND ADDRESS(ES)

AFRL/RXBCM
Dr. David H. Mollenhauer
2941 Hobson Way
Building 654 Room 209
Wright Patterson AFB, OH 45433
DSN 785-9728

10. SPONSOR/MONITOR'S ACRONYM(S)

11. SPONSOR/MONITOR'S REPORT NUMBER(S)

12. DISTRIBUTION / AVAILABILITY STATEMENT

APPROVED FOR PUBLIC RELEASE; DISTRIBUTION UNLIMITED

13. SUPPLEMENTARY NOTES

14. ABSTRACT

This research effort studied the effect of subset size and step size on the spatial resolution and accuracy of Digital Image Correlation (DIC). In addition, DIC was compared with moiré interferometry in an attempt to give future researchers guidance on which method would be appropriate for their research. Strains fields were calculated from displacement fields measured by each method. The strain fields were then compared. The main findings of the research were that: increased subset sizes caused a smoothing of data; increased step sizes reduced the resolution of the data; DIC is an accurate displacement measurement technique; the spatial resolution of DIC is less than that of moiré interferometry; DIC is a highly portable displacement measurement system; DIC is much faster than moiré interferometry.

15. SUBJECT TERMS

Digital Image Correlation, Deformation, Interferometry, Strain (Mechanics), Moiré Effects

16. SECURITY CLASSIFICATION OF:			17. LIMITATION OF ABSTRACT	18. NUMBER OF PAGES	19a. NAME OF RESPONSIBLE PERSON
a. REPORT	b. ABSTRACT	c. THIS PAGE			Dr. Anthony Palazotto AFIT/ENY
U	U	U	UU	113	19b. TELEPHONE NUMBER (Include Area Code) 937-255-3636 x4599